Supplementary Information for

Two-dimensional perovskites with maximum symmetry enable exciton diffusion length exceeding 2 micrometers

Jin Hou[1, #], Jared Fletcher[2, #], Siedah J. Hall[3,4], Hao Zhang[5,6], Marios Zacharias[7], George Volonakis[8], Claire Welton[9], Faiz Mandani[5], Isaac Metcalf[1], Shuo Sun[10], Bo Zhang[10], Yinsheng Guo[10], G. N. Manjunatha Reddy[9], Claudine Katan[8], Jacky Even[7], Matthew Y. Sfeir[3,4], Mercouri G. Kanatzidis[2*] and Aditya D. Mohite[1,5*]

[1]Department of Materials Science and NanoEngineering, Rice University, Houston, Texas 77005, USA.
[2]Department of Chemistry and Department of Materials Science and Engineering, Northwestern University, Evanston, Illinois 60208, USA.
[3]Photonics Initiative, Advanced Science Research Center, City University of New York, New York, 10031, USA
[4]Department of Physics, The Graduate Center, City University of New York, New York, 10016, USA
[5]Department of Chemical and Biomolecular Engineering, Rice University, Houston, Texas 77005, USA.
[6]Applied Physics Graduate Program, Smalley-Curl Institute, Rice University, Houston, TX, 77005, USA.
[7]Univ Rennes, INSA Rennes, CNRS, Institut FOTON - UMR 6082, 35708 Rennes, France.
[8]Univ Rennes, ENSCR, INSA Rennes, CNRS, ISCR (Institut des Sciences Chimiques de Rennes) - UMR 6226, F-35000 Rennes, France.
[9]University of Lille, CNRS, Centrale Lille Institute, Univ. Artois, UMR 8181−UCCS− Unité de Catalyse et Chimie du Solide, F-59000, Lille, France.
[10]Department of Chemistry, University of Nebraska-Lincoln, Lincoln, NE 68588

#Contributed equally

***Correspondence: m-kanatzidis@northwestern.edu, adm4@rice.edu**

Table of Contents

1. Supplementary Text

1.1 Discussion of the Formamidinium (FA) source in the precursors.

Formamidinium Iodide (FAI) could also be used but doesn't work as well as FACl as it sometimes leads to extra formation of δ-phase $FAPbI_3$. Because there is a large excess amount of halide from hydrohalic acid in the solution, the content of halogen in the final perovskites product is only determined by the halide in the hydrohalic acid (e.g. HI acid solution will lead to iodine based perovskites, HBr acid solution will lead to bromine based perovskites, and HI/HBr mixed solution will lead to I/Br perovskite[1]). Here, as long as HI is used as the solvent, it will be the exclusive halide source, and the choice of halogen in the FA source (either FAI, FACl, FABr) or metal source (either PbI_2, $PbCl_2$, $PbBr_2$ or PbO which will become PbX_2, X as a halogen after dissolving) won't influence the final composition.[2]

1.2 Discussion of crystallization kinetics, temperature, and yield of the FA Dion-Jacobson (FA DJ) synthesis.

The crystallization temperature can be further lowered to 100 ˚C (referring to the temperature of hotplate, throughout this section, unless specified otherwise) to increase the yield, but also with more risk of having more $FAPbI_3$ δ-phase in the product as impurity. If the temperature is lower below 100 ˚C, for example room temperature (25 ˚C), the yellow $FAPbI_3$ δ-phase will dominate the crystallization. We think kinetically FA Dion-Jacobson (FA DJ) 2D is much slower in terms of crystallization compared to yellow $FAPbI_3$ δ-phase, which is why high temperatures, longer time strategy is utilized here to have phase-pure $(3AMP)(FA)_{n-1}Pb_nI_{3n+1}$ (FA DJ 2D hereafter, 3AMP=3-(aminomethyl)piperidine). However, as we must crystallize at higher temperatures, we sacrifice the yield since at higher temperatures the solubility of FA DJ 2D in this aqueous solution is higher, leaving a fair amount of precursors still dissolving in the solution. This is also why we use such a large scale of synthesis for these materials.

1.3 Discussion of synthesis of FA DJ powders.

The synthesis of n=1 to n=3 powders are highly reproducible, but we do notice that, when changing between precursor chemicals (for example, from different batches, or from different vendors), or between seasons (there is large variation of humidity in Houston, where synthesis has been performed), occasionally the recipe needs to be slightly adjusted to get phase-pure crystals. The adjustment is simply changing the FACl to 3-(aminomethyl)piperidine (3AMP) (cage cation to spacer cation) ratio. An elevated ratio will lead to higher n and lowering the ratio will lead to lower n. For example, if a n=2 and n=3 mixture is obtained when targeting n=3, slightly adding more FACl and less 3AMP will lead to pure n=3. Based on our experience, this rule is generally applicable to all the 2D halide perovskite synthesis and very useful practically.

For the synthesis of the powder form n=4, this rule holds true; however, there are thermodynamic factors that should be considered. Specifically, when keep rising the ratio of FACl to 3AMP, the formation of n=4 comes at the expense of side product, namely, yellow $FAPbI_3$ δ-phase, and the amount of $FAPbI_3$ δ-phase increases as we further raise the FACl: 3AMP ratio. We think in terms of thermodynamics, the enthalpy of formation[3] (an indicator of whether a 2D perovskite is favorable or not) of $FAPbI_3$ δ-phase will be between FA DJ n=3 and n=4. Therefore, n=4 will be less favorable compared to $FAPbI_3$ δ-phase. However, we could make small but pure n=4 single crystal using our previously reported KCSC method[4], as it enabled us to grow a unfavorable phase over long time via transformation from lower n to higher n.

1.4 Discussion of the temperature-dependent linewidth and exciton-phonon couplings in 2D FA DJ perovskites.

The temperature-dependent PL of FA DJ n=2 and n=3 samples are analyzed by fitting the PL spectra shape with Voigt profiles and extracting their FWHMs as a function of temperature Γ(T). The extracted linewidths are plotted in Fig. 3e. Based on the gradient of the PL linewidths near T = 0K, we estimate that the acoustic phonon contribution to the exciton linewidth broadening is minimal ($\gamma_{ac} < 70$ μeV/K for n=2, and $\gamma_{ac} < 10$ μeV/K for n=3, extracted by taking the gradient $d\Gamma/dT$ at T = 0K).[5] Therefore, we neglect the exciton-acoustic phonon coupling term (behaves linearly with temperature), and fit the temperature-dependent PL broadening by only considering the inhomogeneous broadening and exciton-longitudinal optical (LO) phonon coupling, which is given by:

$$\Gamma(T) = \Gamma_0 + \Gamma_{LO} \frac{1}{e^{E_{LO}/k_B T} - 1}$$

Here, Γ_0 represent the zero-temperature linewidth originating from exciton inhomogeneous broadening, Γ_{LO} represents the strength of exciton-LO phonon coupling, and E_{LO} is the corresponding LO phonon energy. The fitted parameters are shown in Table S2. The extracted LO phonon energies are for ~8meV n=2 and ~18meV for n=3. It suggests that the strength of the electron-phonon coupling in FA DJ n=2 and n=3 is not significantly different than the 3D $FAPbI_3$ phase.

1.5 Discussion of the Solid-state Magic-Angle Spinning Nuclear Magnetic Resonance (MAS NMR) in 2D FA DJ perovskites.

Solid-state NMR (ssNMR) spectroscopy allows the elucidation of the local molecular structures of spacer cations and their interactions with A-site and X-site ions within perovskite slabs, and their packing arrangements. In addition, cation dynamics can be studied by relaxation-based or cross-polarization based techniques.[6–9] The ^1H chemical shifts are sensitive to non-covaletn interactions such as hydrogen bonding or halogen bonding, whereas 207Pb chemical shifts are sensitive to the apical octahedral tilts or Pb-I-Pb bond angles. Specifically, 2D ^1H-^1H exchange spectroscopy (as referred to as spin-diffusion experiments) provide information on through-space proximities between the cage cations and spacer cations. This technique uses different spin-diffusion mixing times synchronized with the rotor period (i.e., integer multiples of sample rotation period), which allow one to probe immediate H-H proximities at sub-nanometer to middle-range proximities of over a nanometer. The on and off-diagonal 2D peaks in such spectra are due to the chemical shifts and through-space proximities, respectively. Intensities of these latter peaks can be adjusted using spin-diffusion mixing time, which allows the spin magnetization to be transferred between the neighboring proton sites in FA and 3AMP cations. A combination of these tools have been used to probe local structures and the cation dynamics in the 2D RP and DJ phases.

1.6 Discussion of pair distribution functions (PDFs) calculated for polymorphous cubic FAPbI3 and tetragonal FA DJ n=2.

The pair distribution functions (PDFs) calculated for polymorphous cubic $FAPbI_3$ and tetragonal FA DJ n=2 is showed in Fig. S20. Atomic contributions from the FA or spacer molecules were excluded from our calculations. Compared to the idealized PDFs obtained from the average atomic

positions related to the high-symmetry cubic Pm3m or tetragonal P4/mmm crystallographic structures (vertical grey dashed lines), the peaks of the PDFs of the polymorphous structures are shifted and broadened, as shown in Fig. S20 (a, c). These effects arise from a distribution of locally disordered unit cells within the polymorphous networks, as seen before in Ref.[10] This approach allows accounting for the random distribution of atomic positions related to slow relaxational motions (Raman scattering, Fig. 4a) By adding thermal disorder due to lattice vibrations (anharmonic phonons) at 300 K (Fig. S20 (b, d)), the PDFs are further broadened, yielding a better comparison with measured PDFs[11].

1.7 Discussion of experimental estimation of exciton diffusion length and diffusivity in n=3 and n=2 DJ FA crystals

Steady state PL diffusion measurements allow extracting exciton diffusion length and diffusivity in 2D materials, by combining PL profiles around the excitation spot and time resolved PL (TRPL) measurements on the same samples.[12] In steady state conditions, the solution of the diffusion equation for the radial distribution of the exciton concentration $n(r)$ corresponds to the convolution between the laser's Gaussian profile and the modified Bessel function of the second kind K_0: $n(r) \propto \int_{-\infty}^{+\infty} K_0\left(\frac{r}{L_D}\right) e^{-(r-r')^2/w^2} dr'$, where L_D is the exciton diffusion length and w is the radius of the laser spot. At some distance away from the laser spot $r \gg L_D$, the modified Bessel function can be approximated by $K_0\left(\frac{r}{L_D}\right) \sim \left(\frac{\pi L_D}{2r}\right)^{1/2} e^{-r/L_D}$ and the convolution by the delta-like Gaussian spot leads to $n(r) \propto \left(\frac{L_D}{r}\right)^{1/2} e^{-r/L_D}$. The L_D value of $1.8\mu m$ ($0.83\mu m$) was estimated from an asymptotic fit at low excitation power respectively for the n=3 (n=2). The exciton diffusivity D_X can then be extracted by combining the exciton diffusion length L_D with the exciton lifetime τ_X deduced from TRPL measurements: $L_D = \sqrt{2 D_X \tau_X}$ (notice that the definition of the diffusivity differs by a factor of $\sqrt{2}$ from the one of ref. [12] to match the definition of ref [13] of the main manuscript).[12] The TRPL signal in the case of the n=3 crystal is better described by a sum of multiexponential components. As the exciton diffusion length is estimated at low excitation power and far away from the laser spot, the relevant exciton lifetime τ_X to estimate the related exciton diffusivity is the long-time TRPL component $\tau_X \sim 3.68 ns$. A high value of the exciton diffusivity is deduced from the present analysis for the n=3 DJ FA compound: $D_X \sim 4.4 cm^2 s^{-1}$.

For the n=2 compound, assuming a similar exciton lifetime, a significantly smaller value of the diffusivity is anticipated $D_X \sim 0.95 cm^2 s^{-1}$.

2. Supplementary Figures

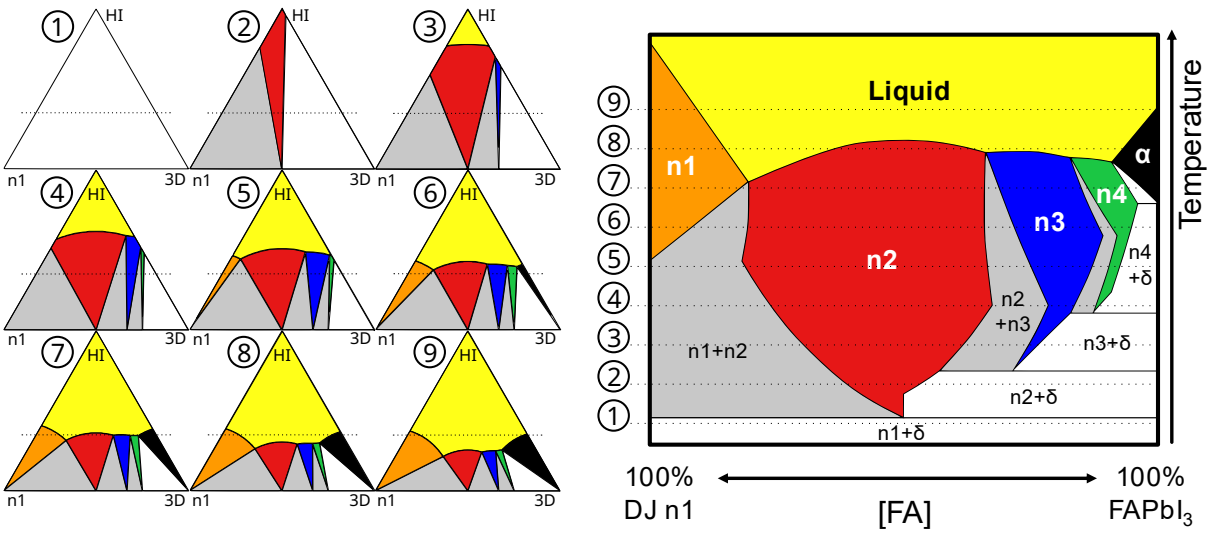

Fig. S1 | The construction of a binary DJ n1 – $FAPbI_3$ phase diagram from ternary DJn1 – $FAPbI_3$ – HI phase diagrams of increasing temperature. A specific concentration of crystals in solution was chosen, represented by the dashed horizontal line across each ternary phase diagram. The intersection of each region of the ternary phase diagram with this line was tracked with temperature to build up the binary phase diagram.

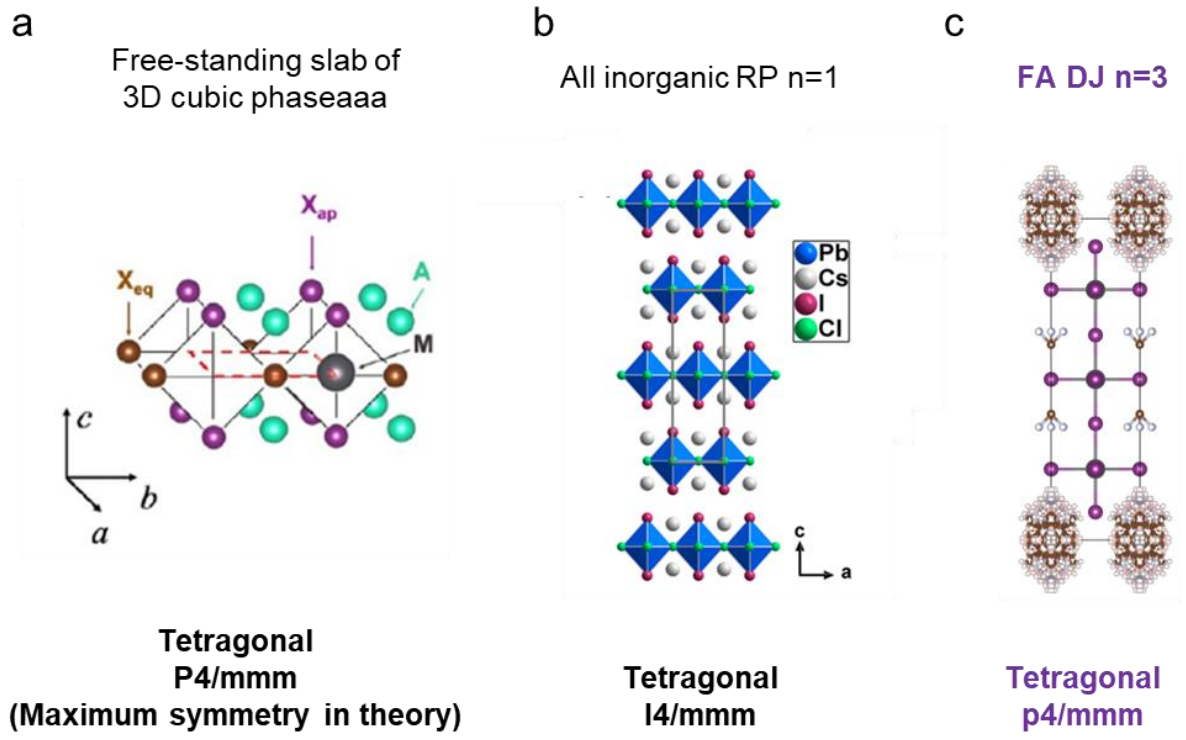

Fig. S2 | Maximum symmetry in 2D halide perovskite. (a) A free-standing slab of 3D cubic phase, adapted from ref. [14], licensed under a Creative Commons Attribution (CC BY) license. (b) The all-inorganic RP n=1 perovskites structure. Adapted with permission from ref. [15]. Copyright 2018 American Chemical Society. (c) The FA DJ n=3 structure.

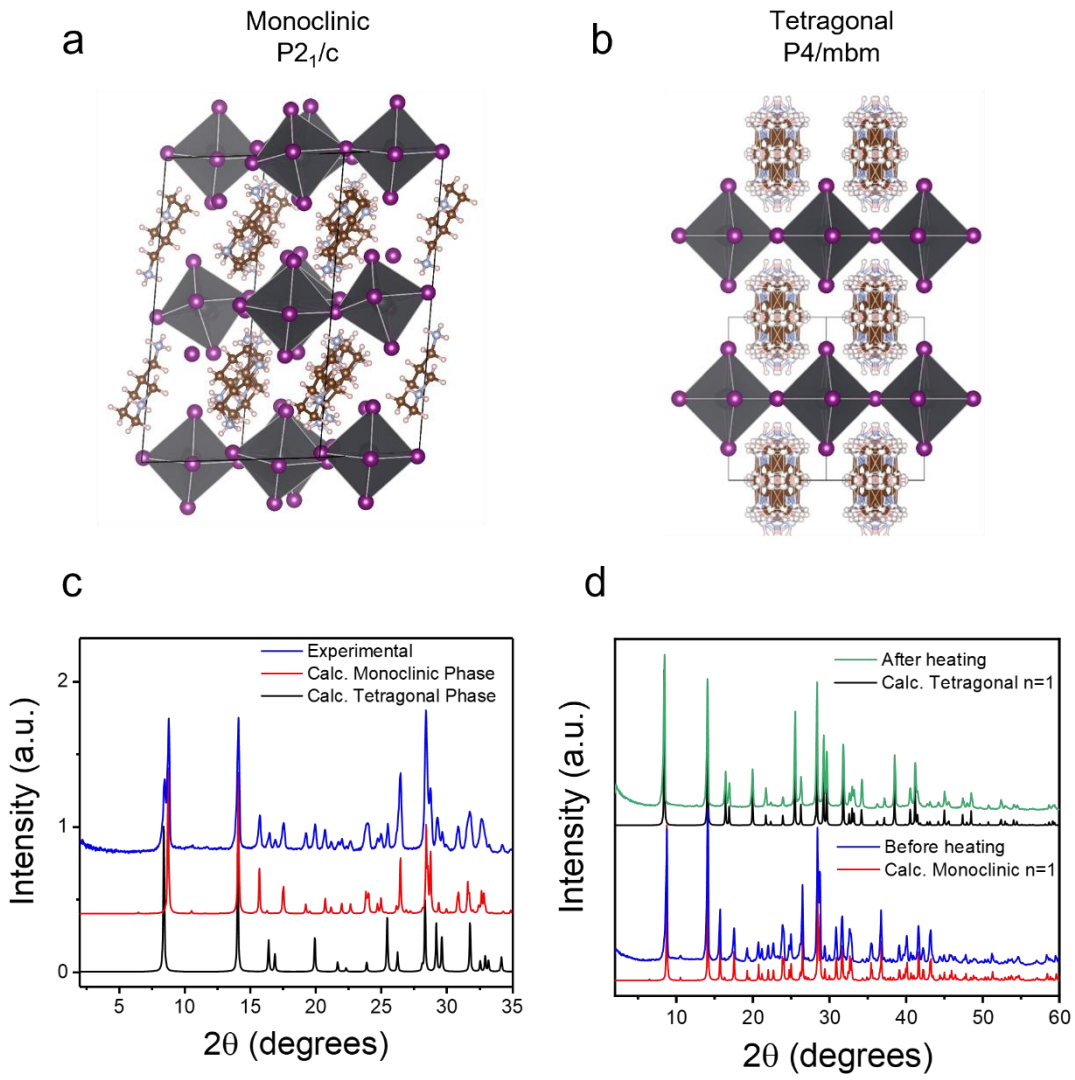

Fig. S3 | Structure of monoclinic and tetragonal DJ n=1. (a) The structure of (a) monoclinic and (b) tetragonal 3-(aminomethyl)piperidine (3AMP) n=1 2D perovskite. (c) The experimental powder X-ray diffraction pattern of DJ n=1 containing mixed monoclinic and tetragonal phases and their corresponding calculated patterns. (d) The experimental powder X-ray diffraction patterns of a pure DJ n=1 monoclinic crystal, before and after heating to 190 °C, and the calculated pattern for monoclinic n=1 and tetragonal n=1.

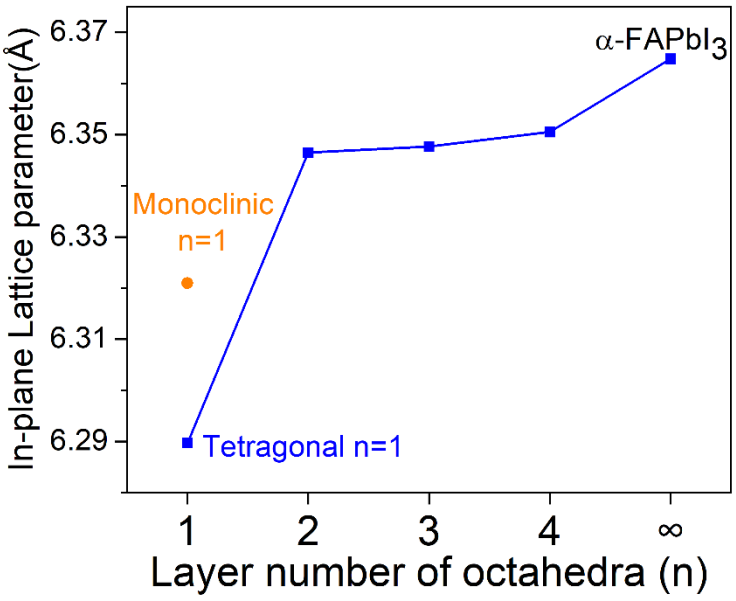

Fig. S4 | The in-plane lattice parameters of 2D FA DJ perovskites.

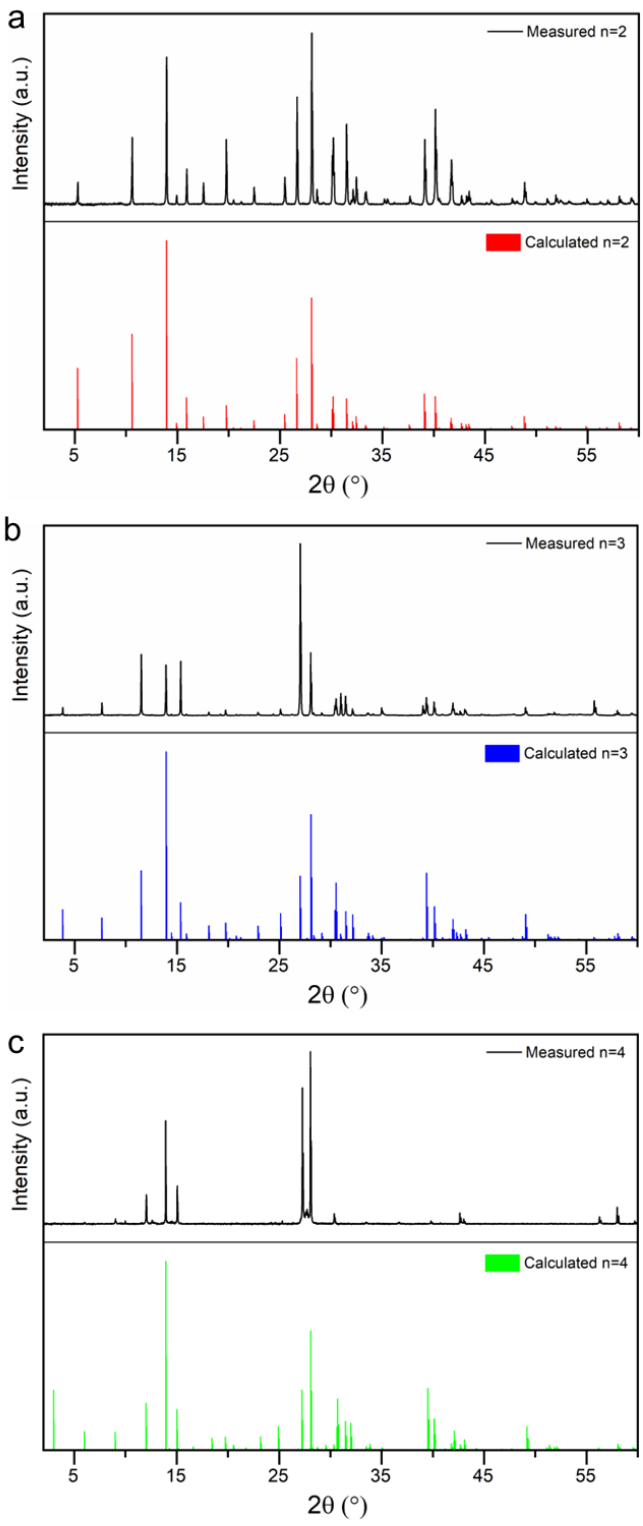

Fig. S5 | Experimental and calculated powder X-ray pattern of FA DJ (a) n=2, (b) n=3 and (c) n=4.

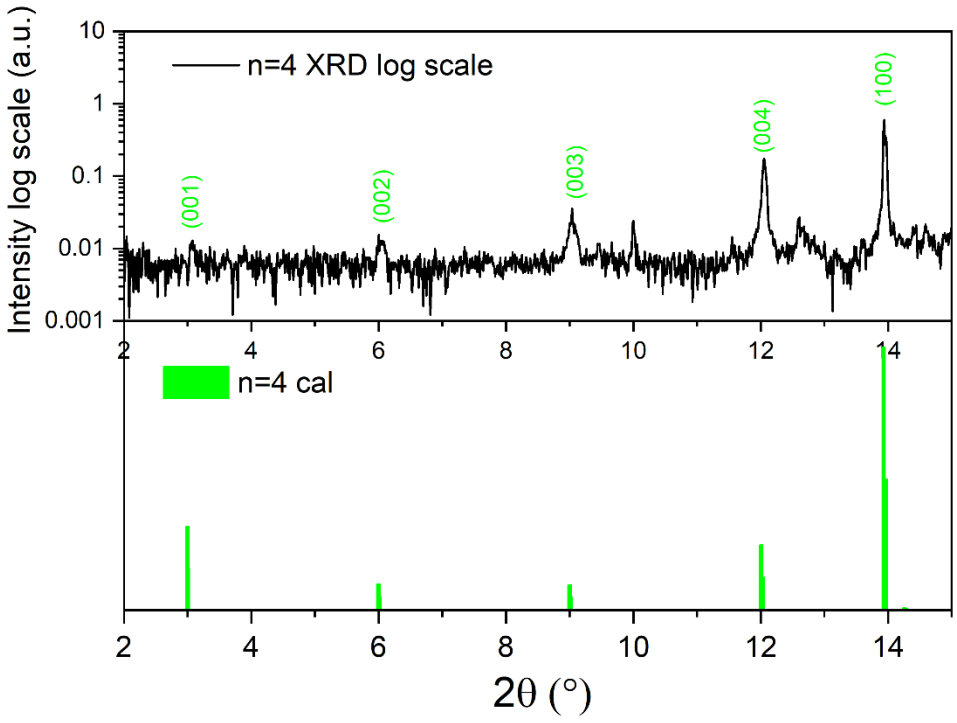

Fig. S6 | PXRD of FA DJ n=4 at low angle, log-scaled intensity.

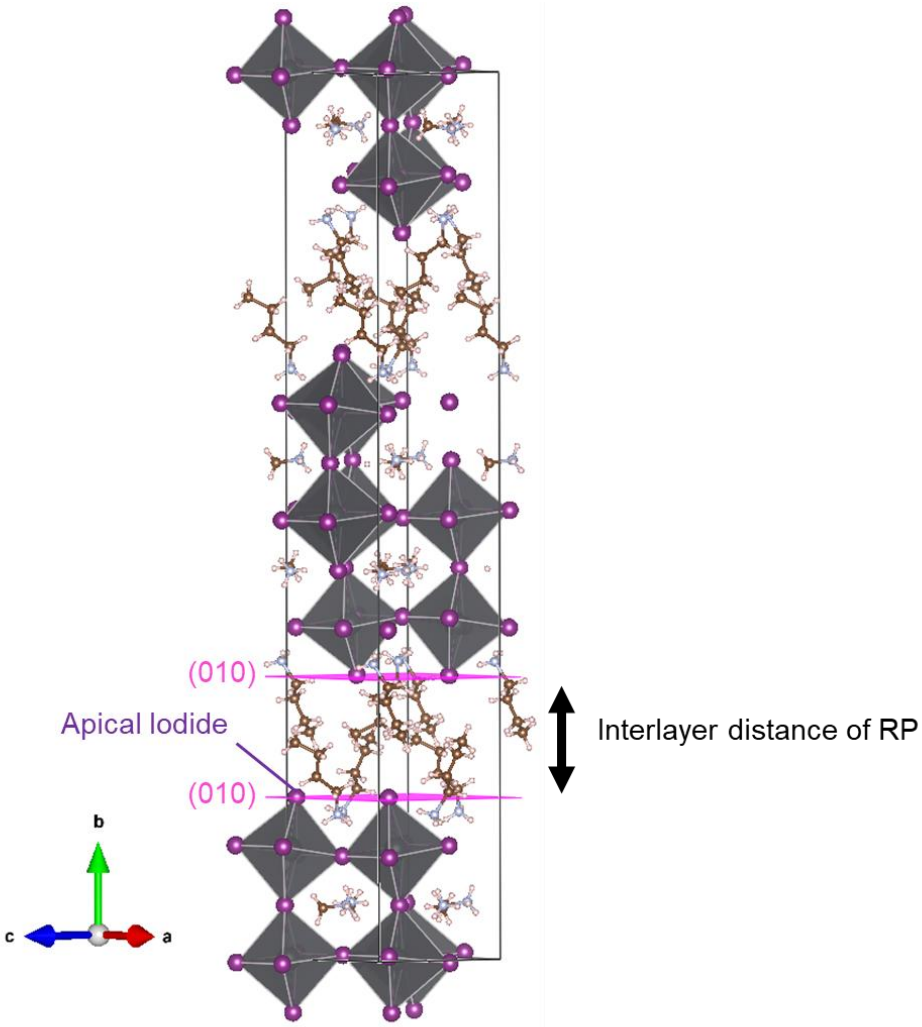

Fig. S7 | Interlayer distance for RP BA phase.

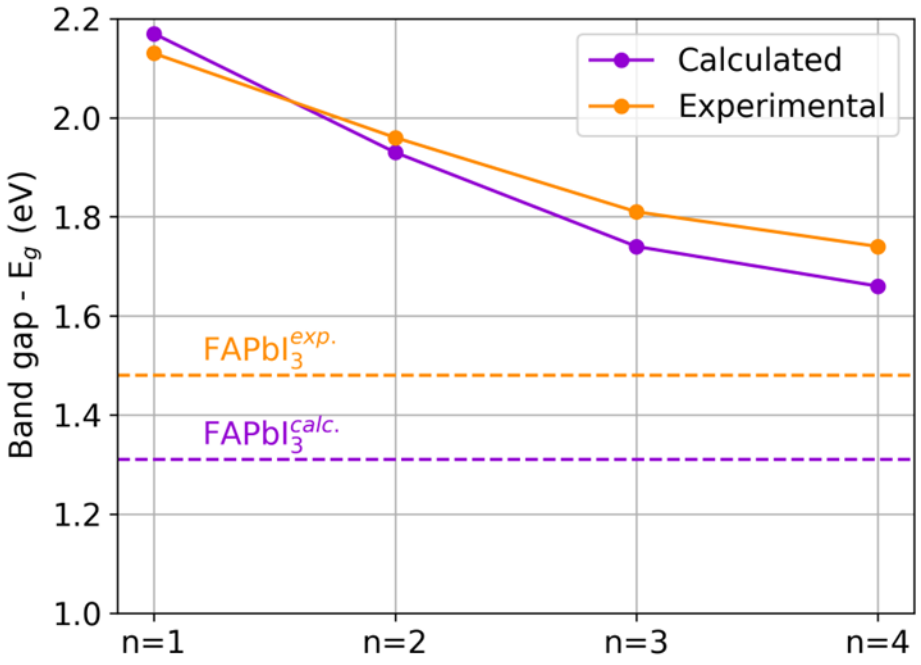

Fig. S8 | Experimental optical and calculated electronic bandgaps for the FA DJ layered compounds. We applied a rigid scissor shift of 0.24 eV estimated for $FAPbI_3$ to account for the effects of polymorphism on the 2D FA DJ series.

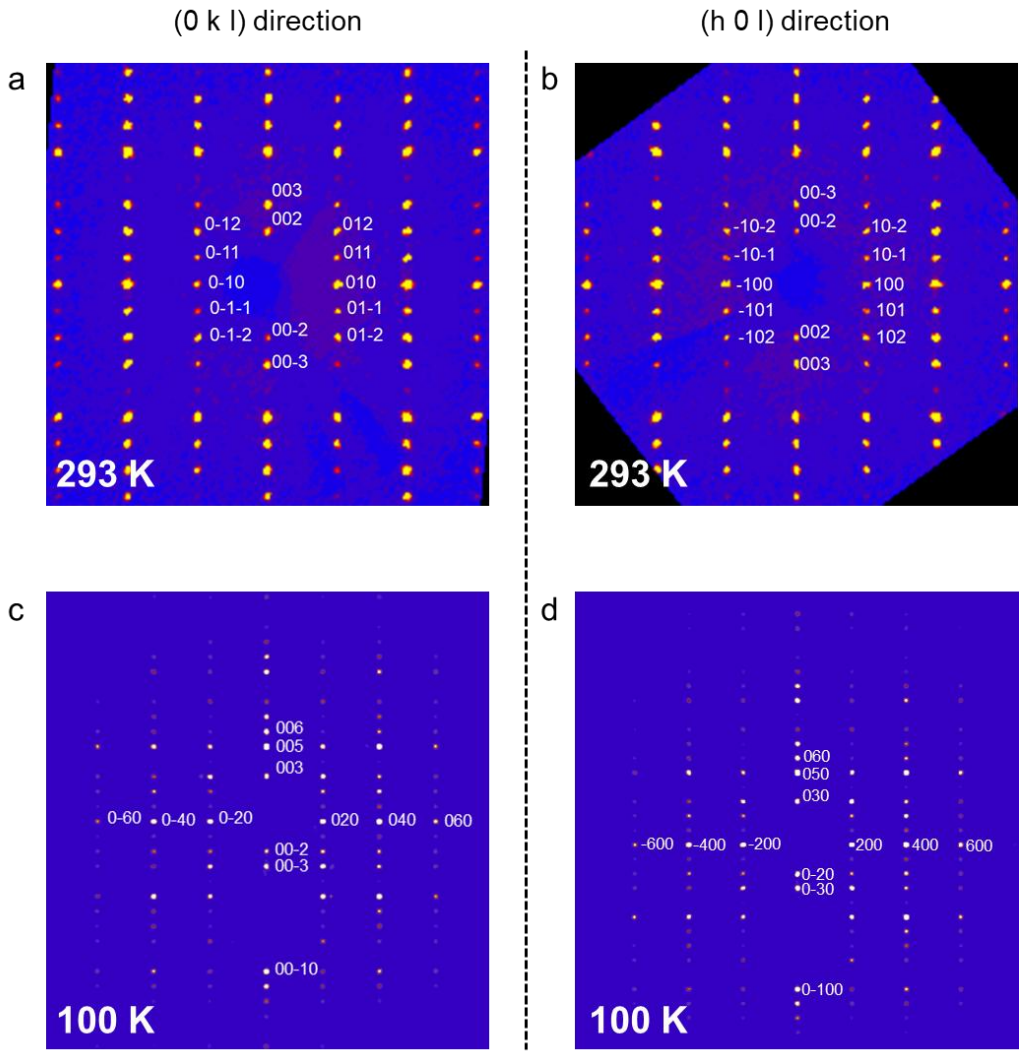

Fig. S9 | Procession images of FA DJ n=2, (a) along (0 k l) direction and (b) along (h 0 l) direction at Room temperature (293K), (c) along (0 k l) direction and (d) along (h 0 l) direction at low temperature (100K).

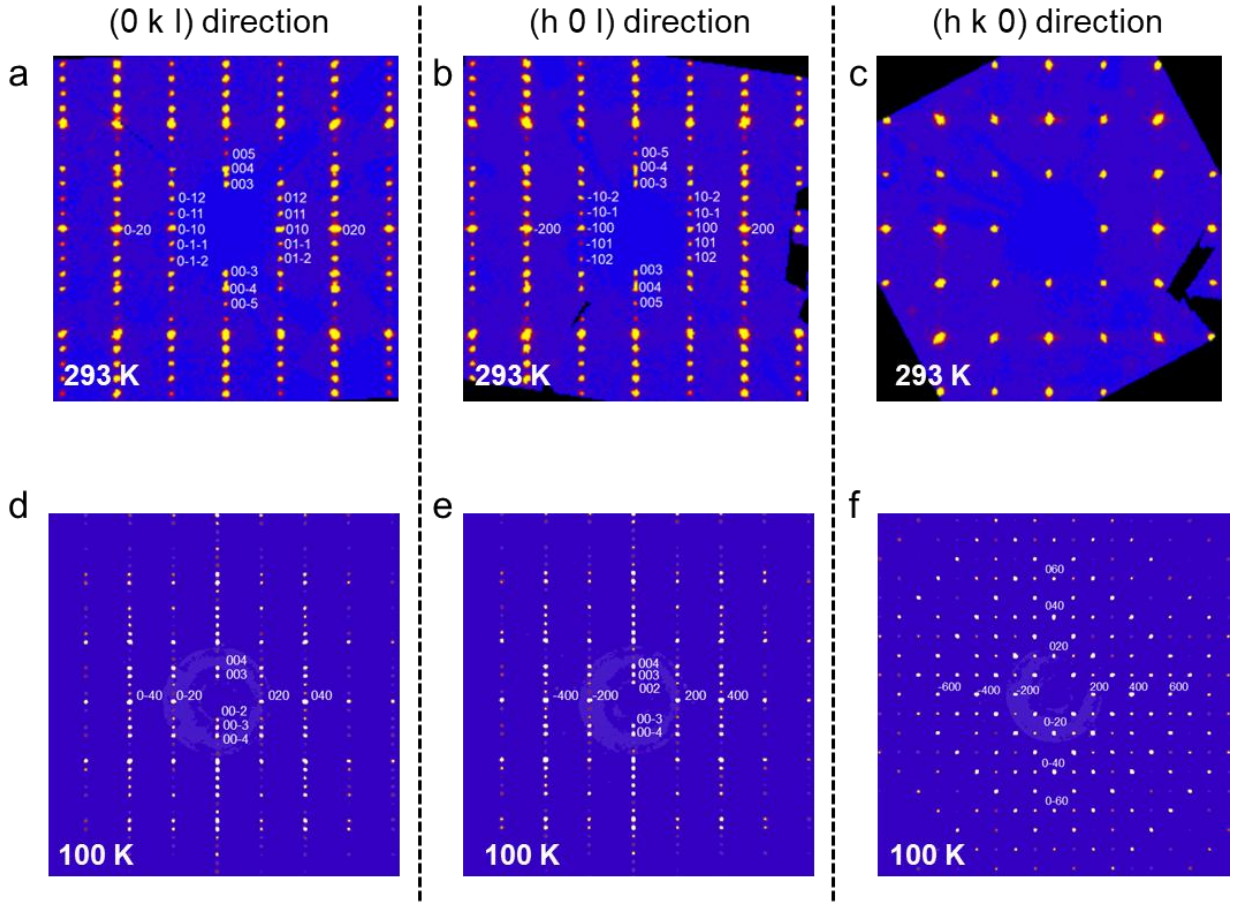

Fig. S10 | Procession images of FA DJ n=3, (a) along (0 k l) direction, (b) along (h 0 l) direction, and (c) along (h k 0) direction, at Room temperature (293K), (d) along (0 k l) direction, (e) along (h 0 l) direction, and (f) along (h k 0) direction, at low temperature (100K).

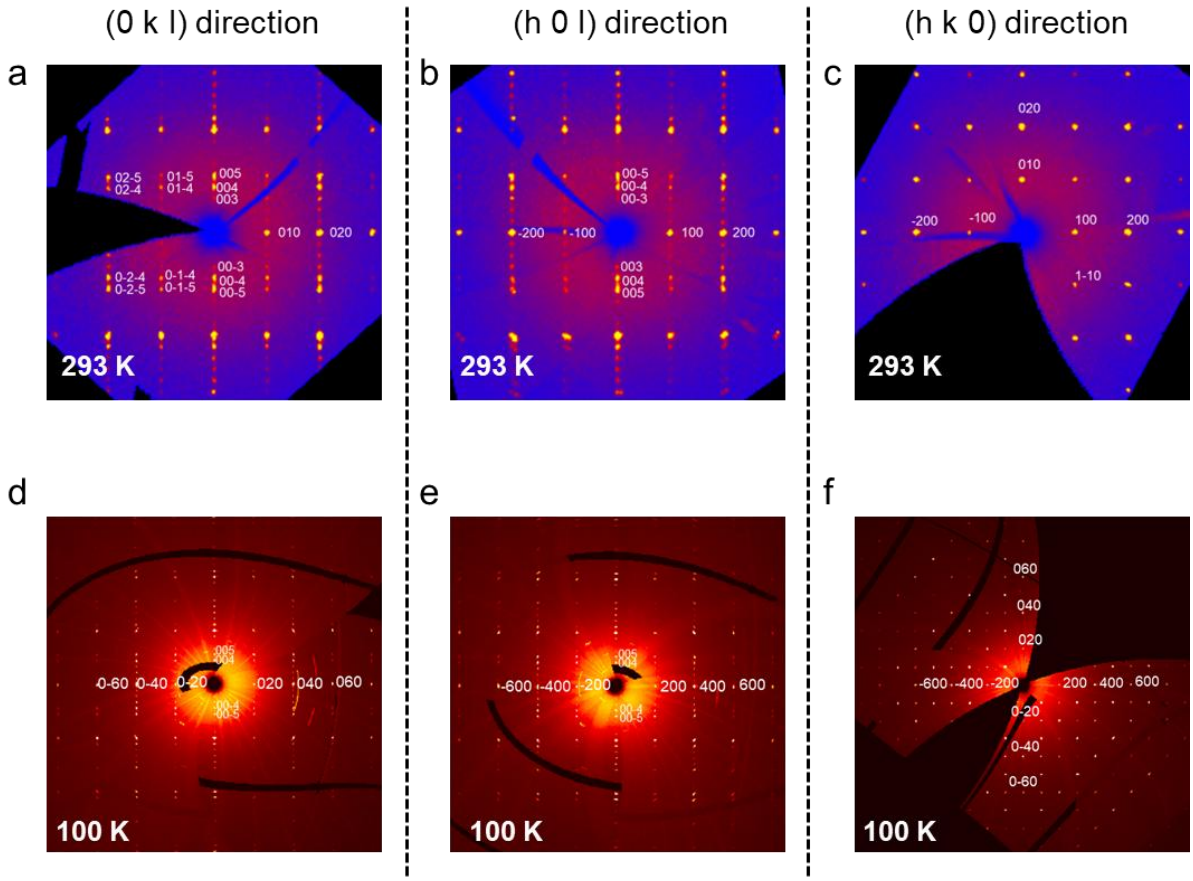

Fig. S11 | Procession images of FA DJ n=4, (a) along (0 k l) direction, (b) along (h 0 l) direction, and (c) along (h k 0) direction, at Room temperature (293K), (d) along (0 k l) direction, (e) along (h 0 l) direction, and (f) along (h k 0) direction, at low temperature (100K).

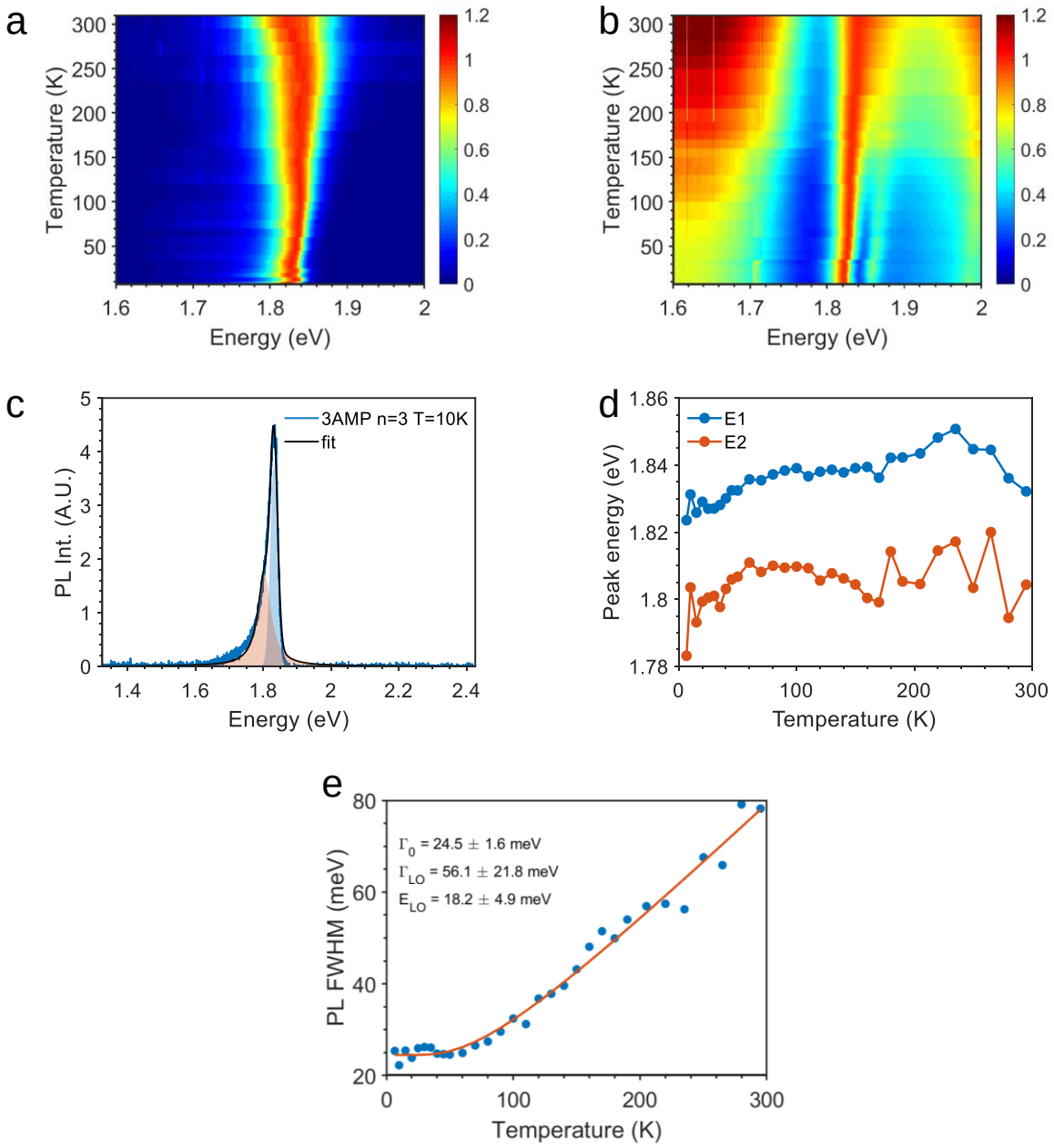

Fig. S12 | PL broadening analysis of FA DJ n=3. (a) Normalized steady-state photoluminescence (PL) profile of FA DJ n=3 at temperatures between 6 to 300K. (b) Temperature dependent reflectance spectrum of FA DJ n=3. (c) The raw data and fitting of PL of FA DJ n=3 at 10 K. (d) The extracted peak energy evolution as a function of temperature for free exciton (E1) and bound exciton (E2) states. (e) Temperature-dependent PL FWHM of FA DJ n=3, and the fitting parameters.

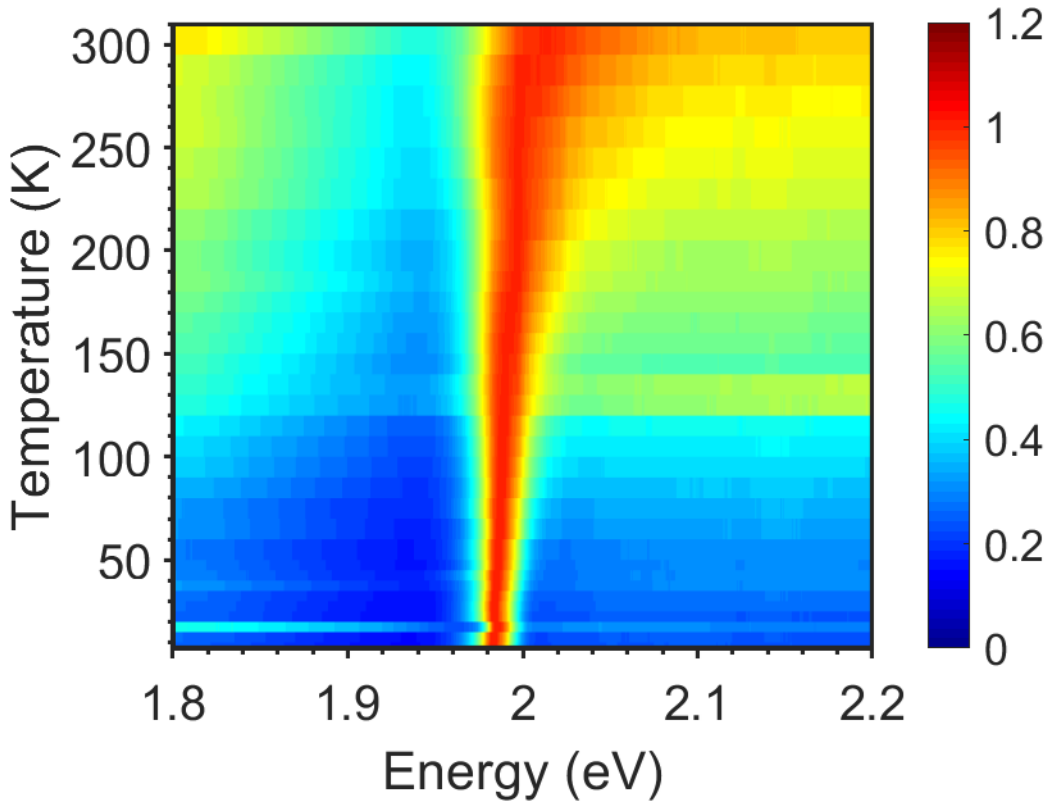

Fig. S13 | Temperature dependent reflectance spectrum of FA DJ n=2

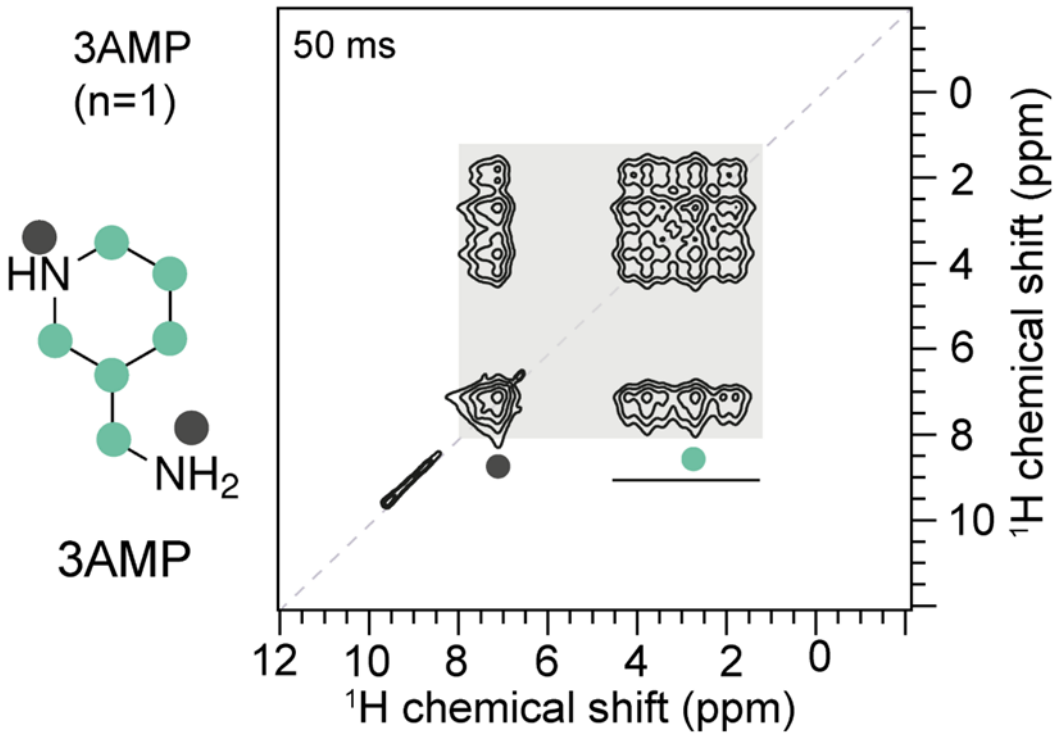

Fig. S14 | 2D ^{1}H-^{1}H spin-diffusion NMR spectra of layered DJ n=1 with a schematic of the 3AMP cation with color dots aiding the spectral analysis.

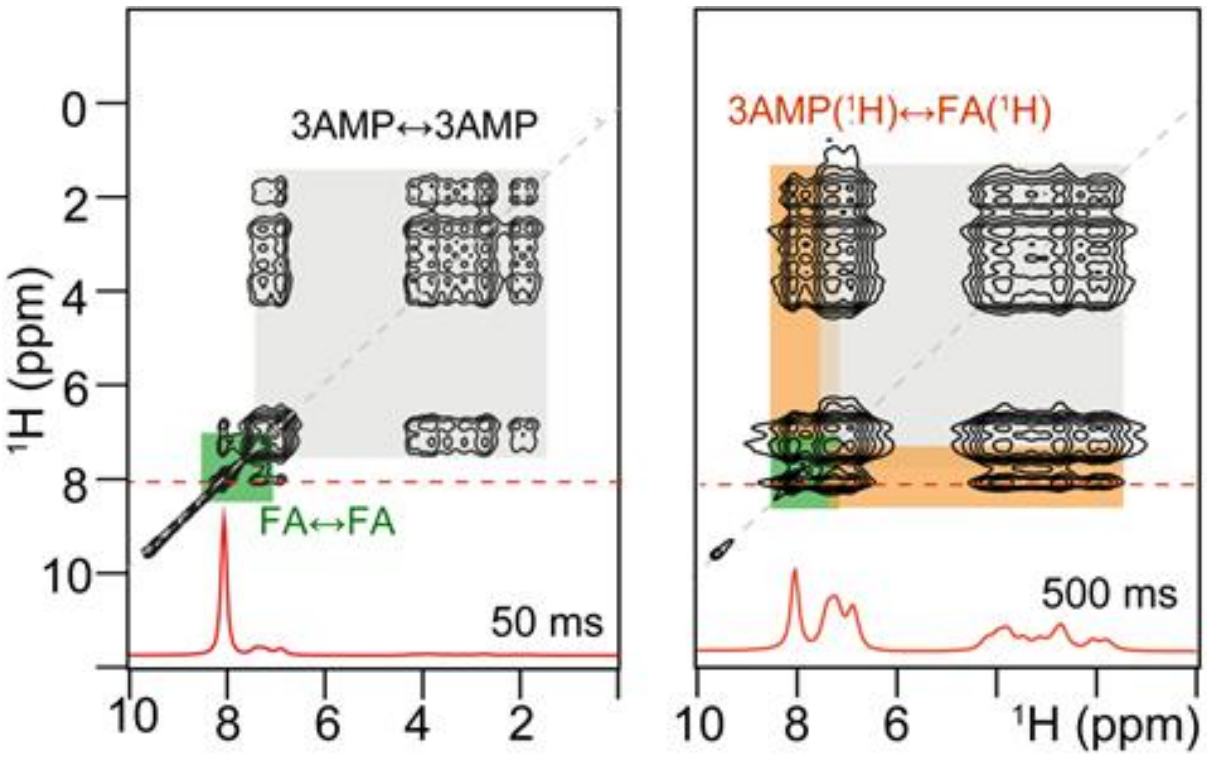

Fig. S15 | 2D ^{1}H-^{1}H spin-diffusion NMR spectra of FA DJ n=2 2D ^{1}H-^{1}H spin-diffusion NMR spectra of FA DJ n=2 acquired at 21.1 T (^{1}H = 900 MHz), room temperature, and 50 kHz MAS using 50 ms (**left**) and 500 ms (**right**) of spin-diffusion mixing time, with the 1D ^{1}H NMR spectra plotted on the horizontal projections..

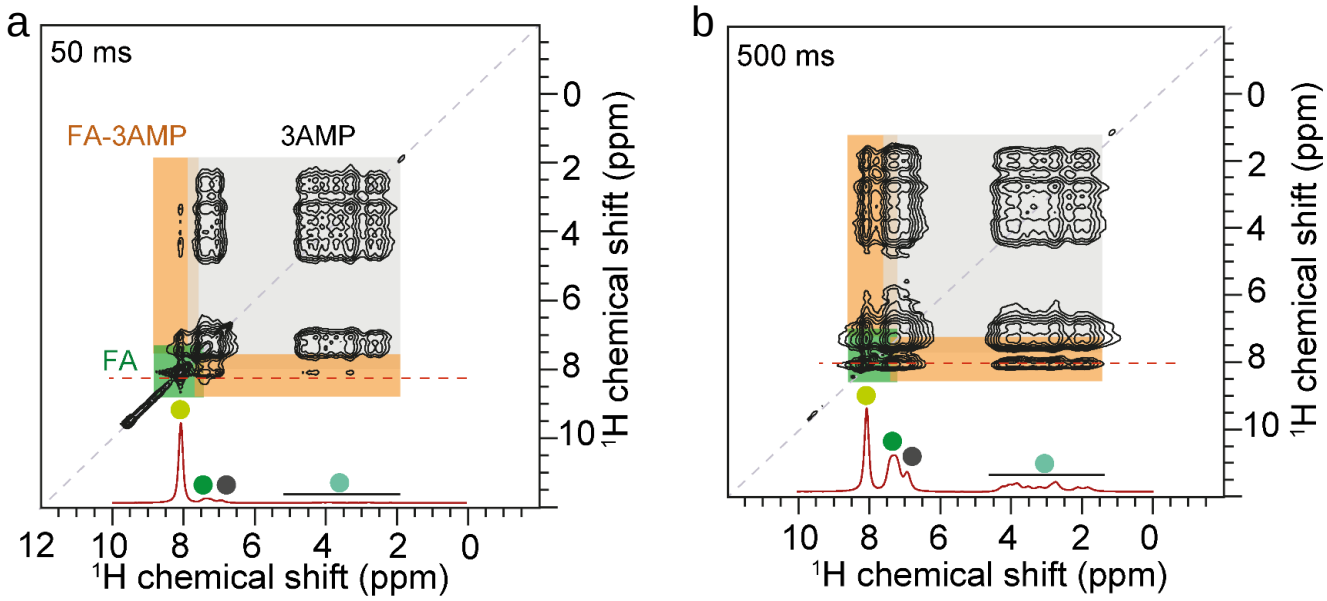

Fig. S16 | 2D ^{1}H-^{1}H spin-diffusion NMR spectra of FA DJ n=3 acquired at 21.1 T (^{1}H = 900 MHz), room temperature, and 50 kHz MAS using 50 ms (**a**) and 500 ms (**b**) of spin-diffusion mixing time, with the 1D ^{1}H NMR spectra plotted on the horizontal projections.

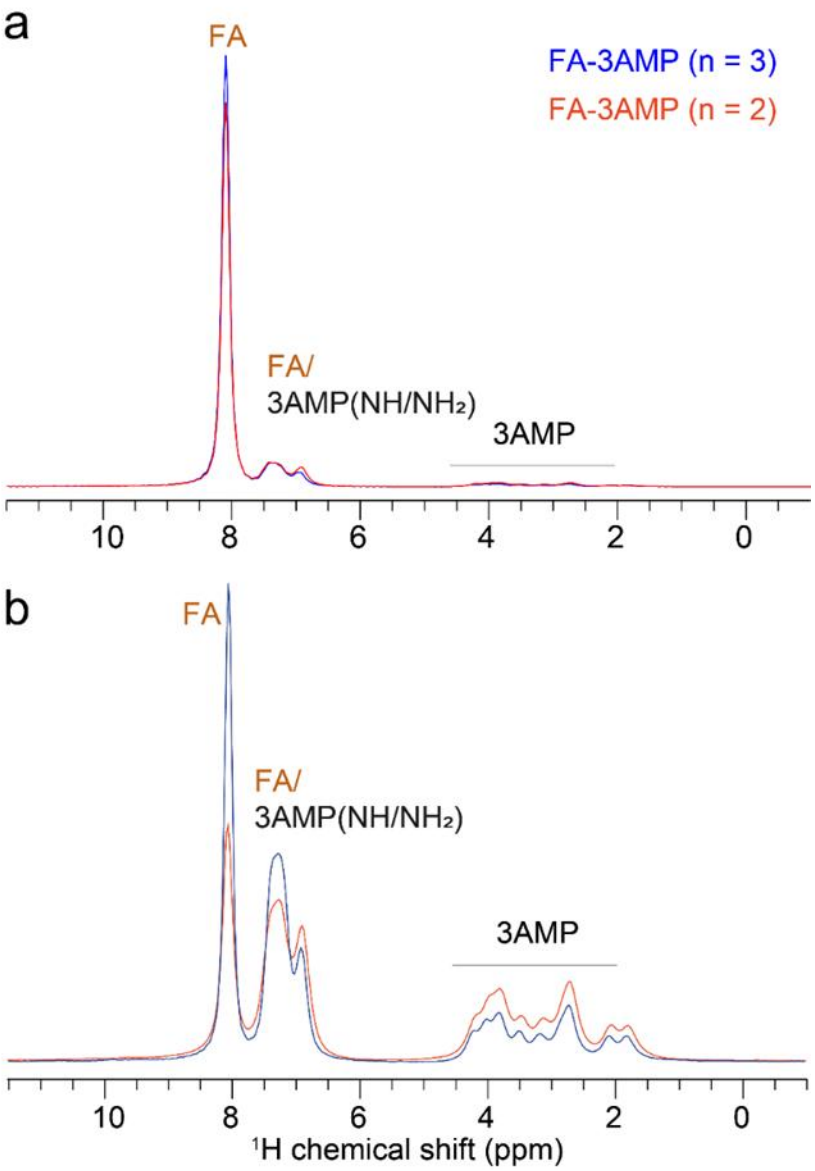

Fig. S17 | Line-cut row ^{1}H spectra obtained of FA DJ. Line-cut row ^{1}H spectra obtained of FA DJ from the 2D ^{1}H-^{1}H spin diffusion NMR spectra of FA 3AMP DJ phases obtained with (a) 50 ms and (b) 500 ms at a ^{1}H chemical shift of 8.2 ppm (FA, NH). The spectra of n=2 and n=3 phases are depicted in red and blue colors, respectively. All spectra were acquired at 21.1 T (^{1}H = 900 MHz), room temperature, and 50 kHz MAS.

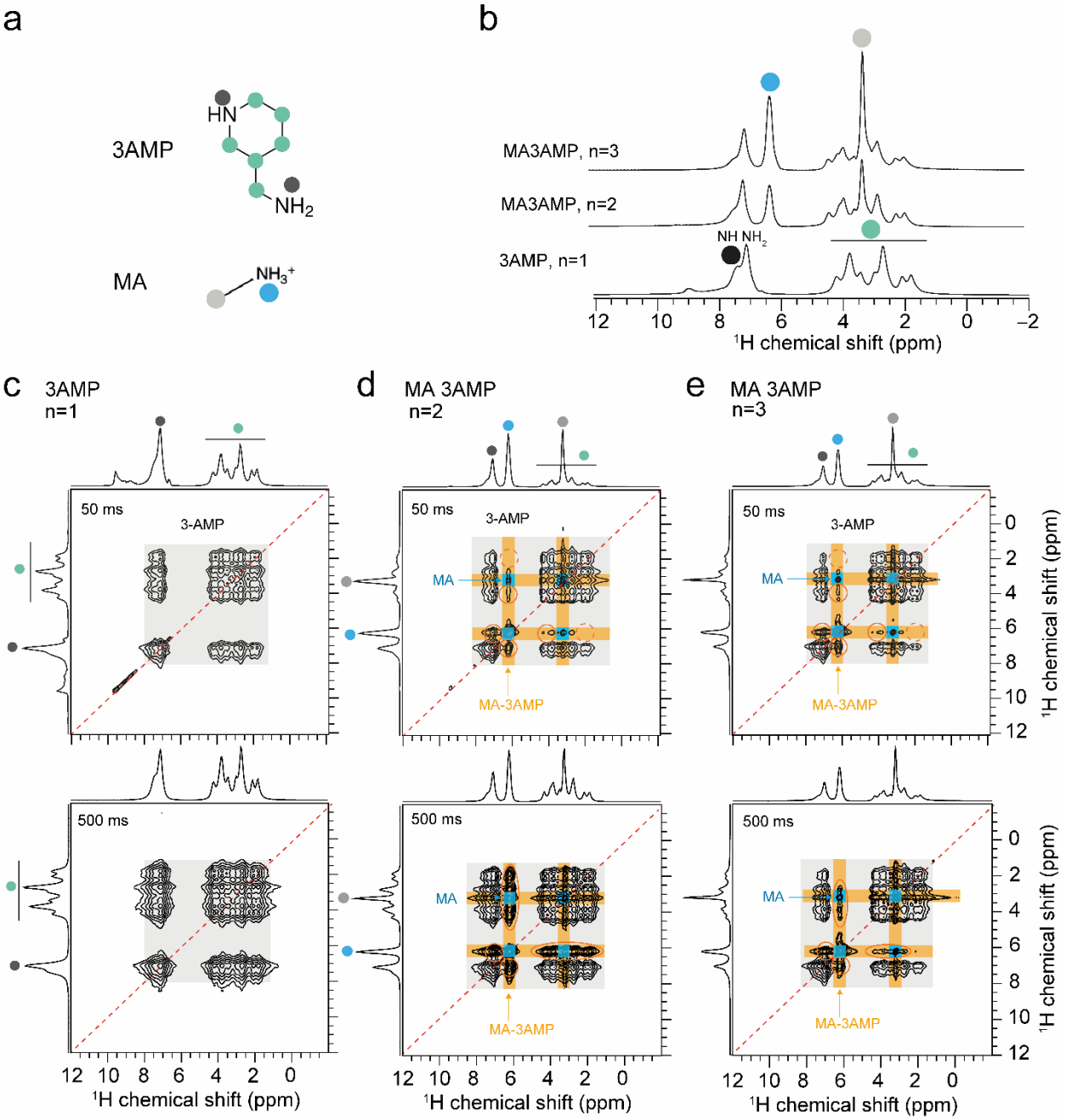

Fig. S18 | NMR analysis of Methyl ammonium (MA) DJ 2D perovskite. (a) Schematic of 3AMP and MA cations as color dots to aid spectral interpretation. (b) solid-state 1D 1H NMR spectra of layered DJ phases as indicated. Solid-state 2D 1H-1H SD NMR spectra of layered DJ phases: (c) DJ n=1, (d) MA DJ n=2, and (e) MA DJ n=3 acquired with 50 ms (top) and 500 ms (bottom) of spin diffusion time. Peaks corresponding to the 3AMP spacer and MA cations are depicted in gray and blue boxes. All spectra were acquired at 21.1 T (1H = 900 MHz), room temperature, and 50 kHz MAS.

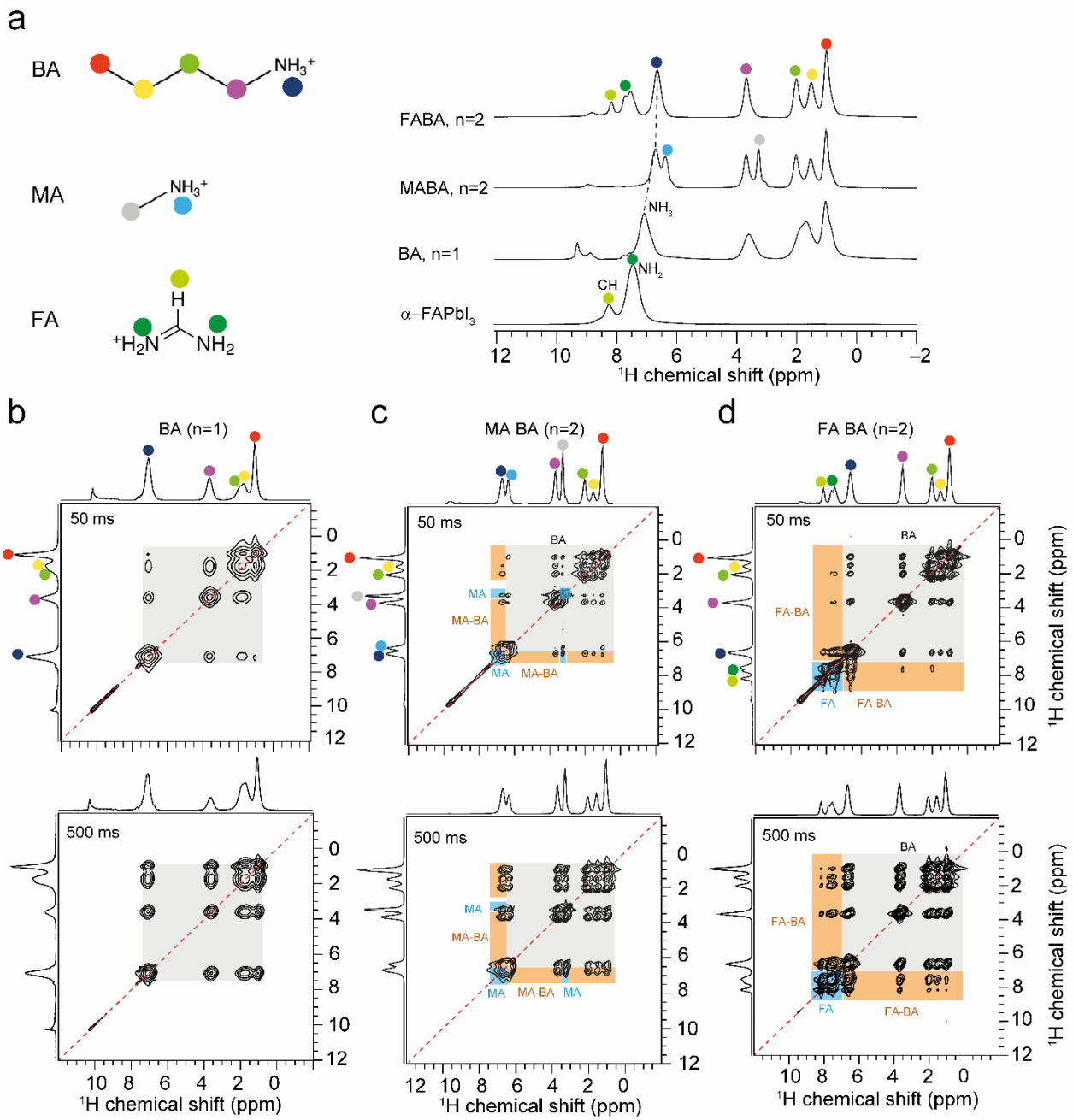

Fig. S19 | NMR analysis of MA BA and FA BA 2D perovskite. (a) Schematic of 3AMP and MA cations as color dots. Solid-state (b) 1D NMR spectra of RP phases and 3D perovskites as indicated alongside a schematic of the BA and FA cations with color dots aiding the spectral analysis. 2D 1H-1H spin-diffusion NMR spectra of (c) $(BA)PbI_4$ (n=1), (d) MA BA (n=2), and (e) FA BA (n=2) acquired with 50 ms (top) and 500 ms (bottom) of spin diffusion time, together with the 1D 1H NMR spectra plotted on the horizontal and vertical projections. All spectra were acquired at 21.1 T (1H = 900 MHz), room temperature, and 50 kHz MAS.

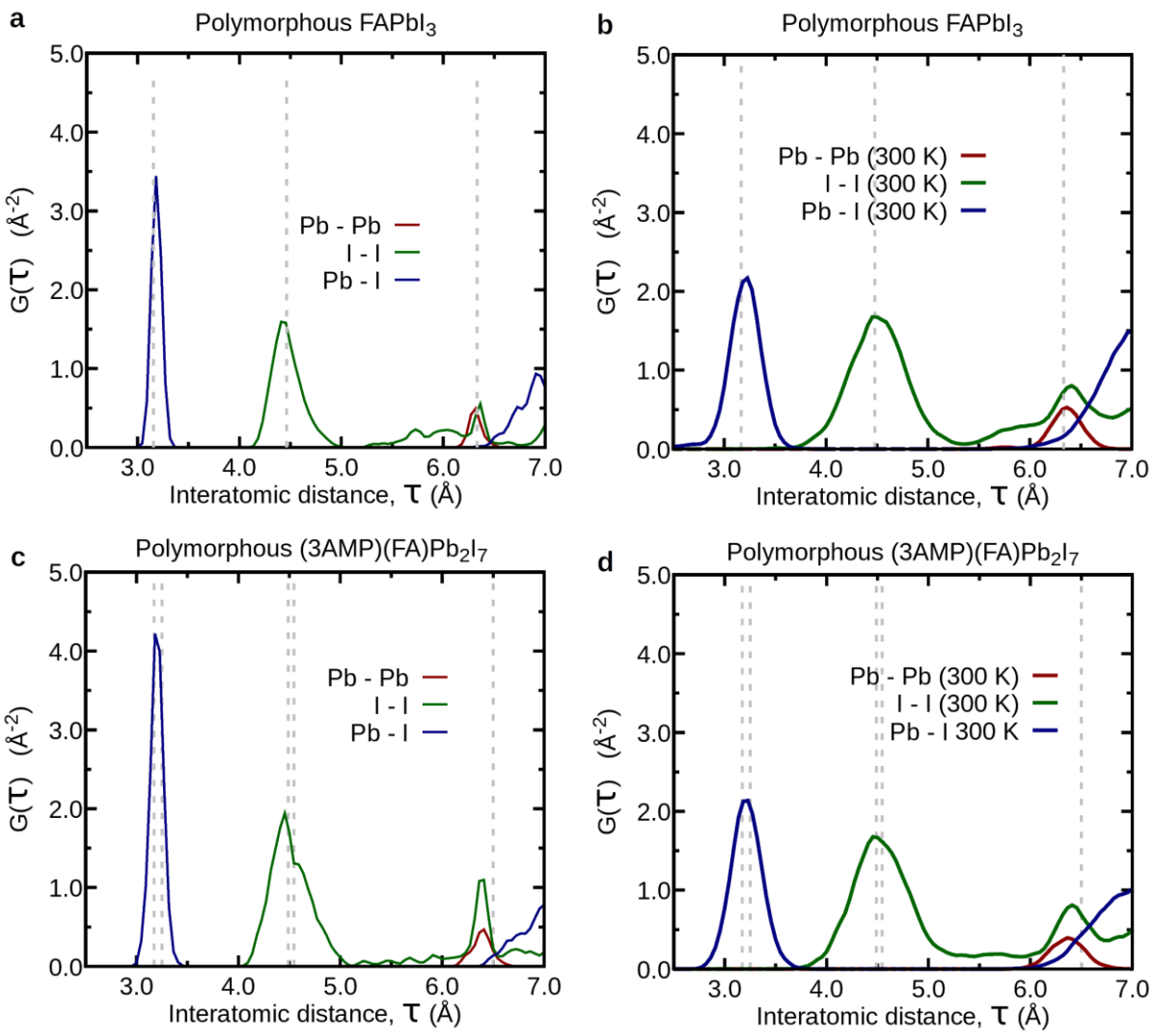

Fig. S20 | Pair distribution function (PDF) of FA DJ and 3D $FAPbI_3$. (a,b) Pair distribution function (PDF) of polymorphous cubic $FAPbI_3$ without (a) and with (b) the effect of lattice vibrations at 300 K. Vertical dashed lines represent pair distribution functions of the monomorphous (high-symmetry) $FAPbI_3$. (c,d) As in (a,b) but for FA DJ n=2.

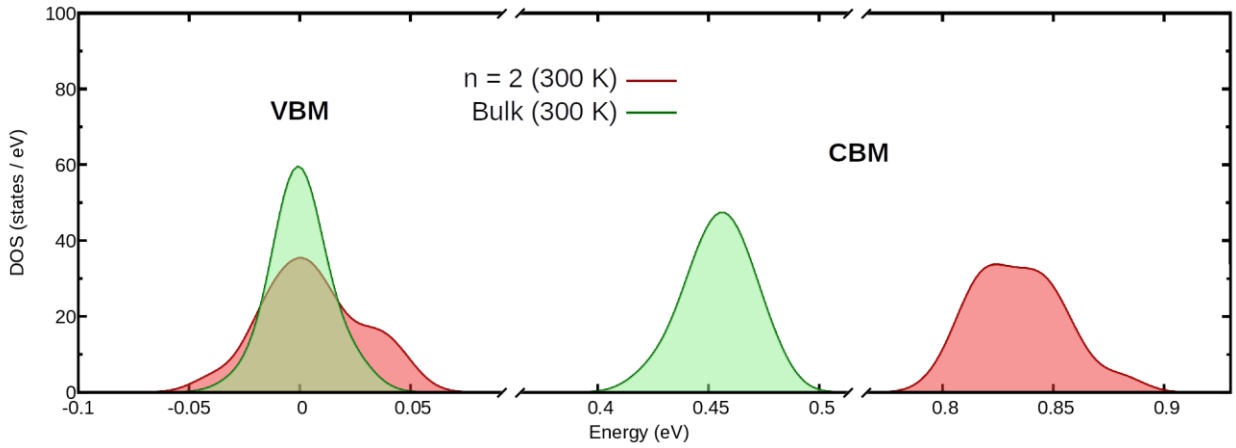

Fig. S21 | DOS of FA DJ and 3D $FAPbI_3$. DFT-PBEsol density of states (DOS) at the valence band maximum (VBM) and conduction band minimum (CBM) of polymorpous FA DJ n=2 (red) and $FAPbI_3$ (green). Calculations include the effect of electron-phonon coupling at 300 K.

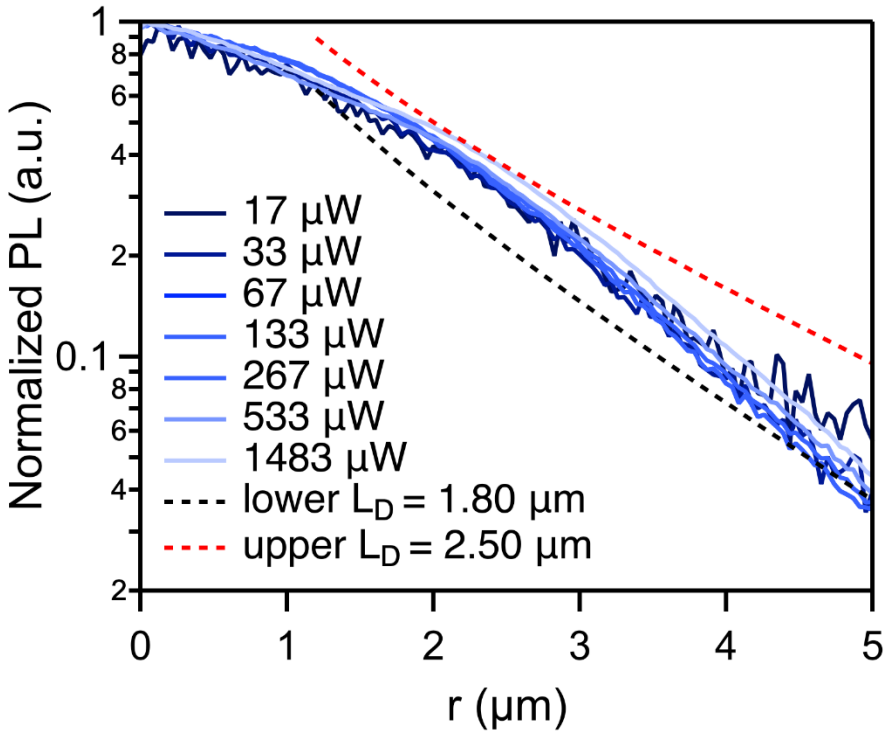

Fig. S22 | Diffusion lengths derived from fitting of normalized spatial PL profiles of FA DJ n=3

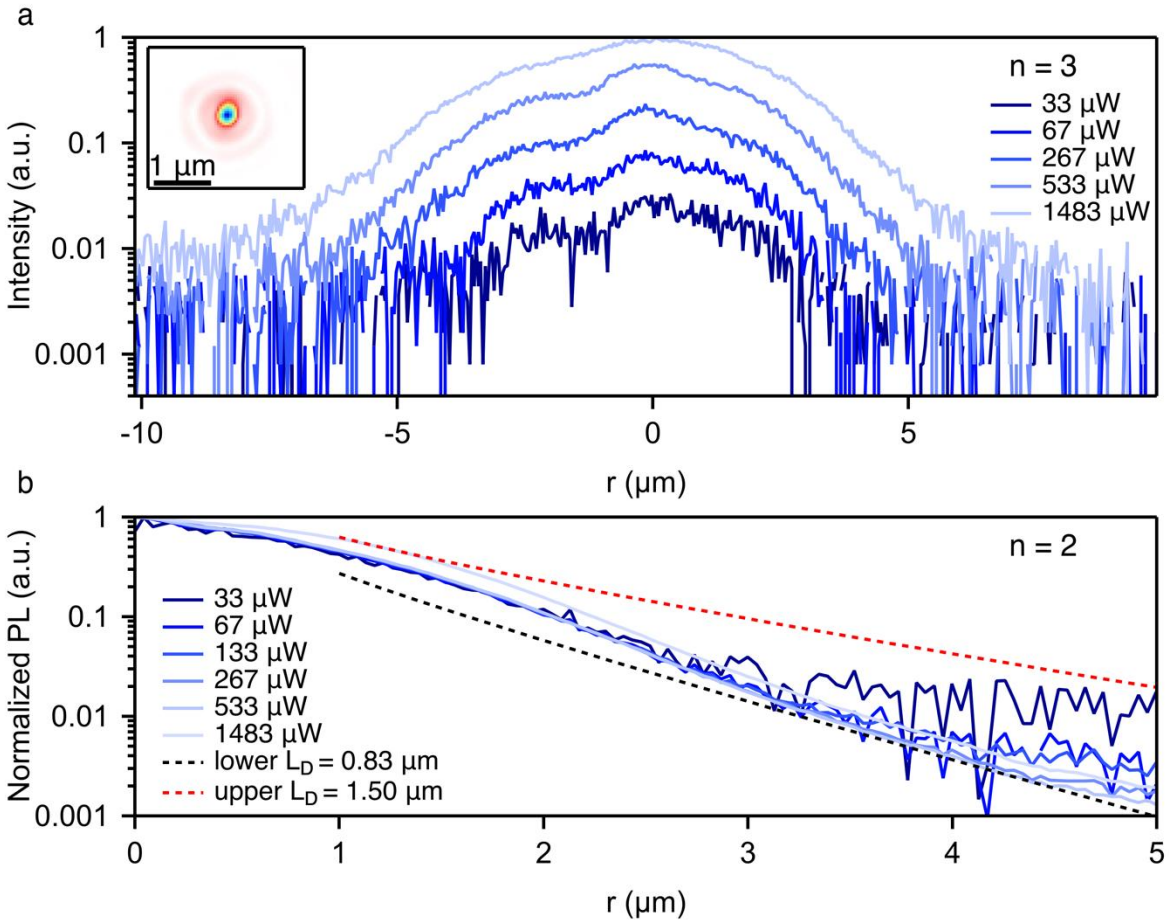

Fig. S23 | FA DJ diffusion length analysis. (a) Power dependent diffusion profiles cut from FA DJ n=3 real-space PL images. Inset shows reflection of 532 nm laser with ~ 0.6 µm spot size. (b) Normalized PL intensities for FA DJ n=2 where upper (red) and lower (black) bound diffusion length fittings are 1.5 µm and 0.83 µm respectively.

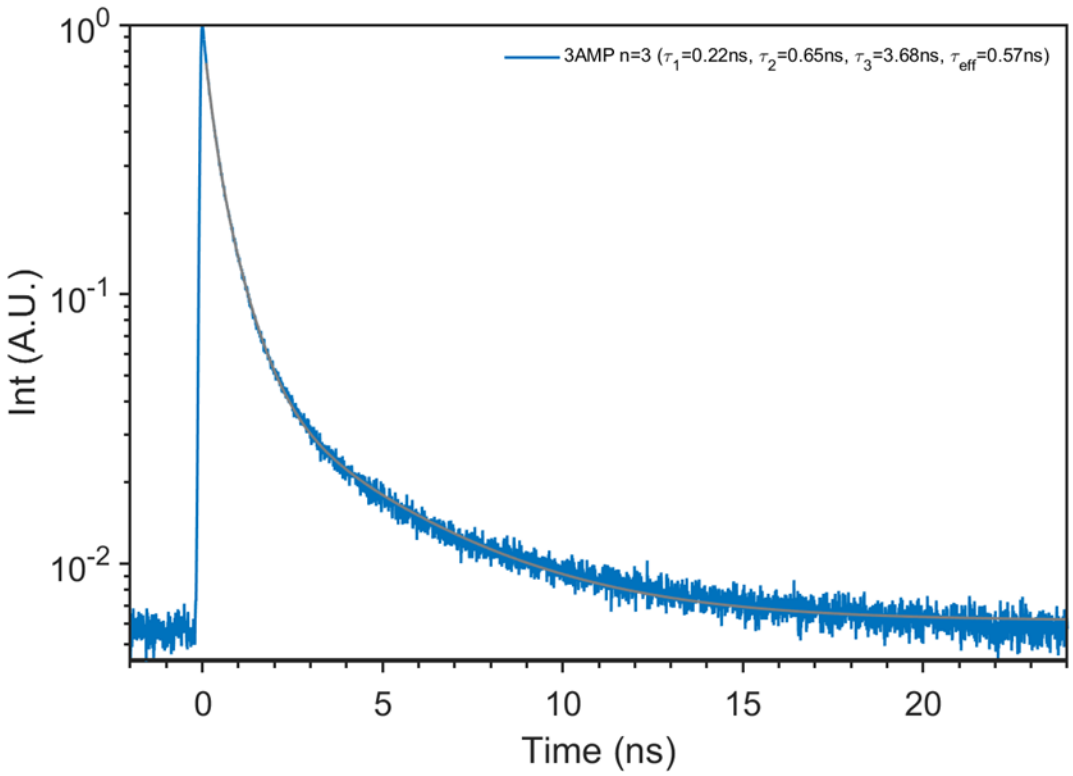

Fig. S24 | Time-resolved photoluminescence spectroscopy (TRPL) of FA DJ n=3 crystal flake. The PL was spectrally selected at exciton emission at 680nm, showing non-exponential decay traces which are fitted with triple exponential decay curves (τ_1 = 0.22 ns, τ_2 = 0.65 ns, τ_3 = 3.68 ns) with average lifetime τ = 0.57 ns.

3. Supplementary Table

Table S1 | Crystal Data and Structure Refinement for $(3AMP)(FA)_{n-1}Pb_nI_{3n+1}$, n=1 to n=4.

Compound				
	$(3AMP)PbI_4$	$(3AMP)(FA)Pb_2I_7$	$(3AMP)(FA)_2Pb_3I_{10}$	$(3AMP)(FA)_3Pb_4I_{13}$
Empirical formula	C6 H16 I4 N2 Pb	C7 H16 I7 N4 Pb2	C8 H16 I10 N6 Pb3	C9 H16 I13 N8 Pb4
Formula weight	831.00	1458.92	2086.84	2714.76
Temperature	285(14) K	293 K	293 K	293 K
Wavelength	0.71073 Å	0.56083 Å	0.56083 Å	0.56083 Å
Crystal system	Tetragonal	Tetragonal	Tetragonal	Tetragonal
Space group	P4/mbm	P4/mmm	P4/mmm	P4/mmm
Unit cell dimensions	a = 8.8950(2) Å, α = 90° b = 8.8950(2) Å, β = 90° c = 10.4829(4) Å, γ = 90°	a = 6.3465(9) Å, α = 90° b = 6.3465(9) Å, β = 90° c = 16.722(3) Å, γ = 90°	a = 6.3477(9) Å, α = 90° b = 6.3477(9) Å, β = 90° c = 23.054(5) Å, γ = 90°	a = 6.3505(9) Å, α = 90° b = 6.3505(9) Å, β = 90° c = 29.454(6) Å, γ = 90°
Volume	829.42(5) $Å^3$	673.5(2) $Å^3$	928.9(3) $Å^3$	1187.9(4) $Å^3$
Z	2	1	1	1
Density (calculated)	3.327 g/cm^3	3.597 g/cm^3	3.730 g/cm^3	3.795 g/cm^3
Absorption coefficient	17.588 mm^{-1}	10.946 mm^{-1}	11.686 mm^{-1}	12.070 mm^{-1}
F(000)	720	621	882	1143
θ range for data collection	3.239 to 29.988°	1.922 to 24.992°	2.091 to 24.987°	2.182 to 19.981°
Index ranges	-12<=h<=12, -12<=k<=10, -14<=l<=14	-9<=h<=9, -9<=k<=9, -25<=l<=24	-9<=h<=9, -9<=k<=9, -34<=l<=34	-7<=h<=7, -7<=k<=7, -35<=l<=35
Reflections collected	14588	15960	29086	9528
Independent reflections	694 [R_{int} = 0.0232]	796 [R_{int} = 0.0677]	1086 [R_{int} = 0.0406]	773 [R_{int} = 0.1328]
Completeness to θ = 25.242°	99.8%	99.8%	98.6%	99.3%
Refinement method	Full-matrix least-squares on F^2	Full-matrix least-squares on F^2	Full-matrix least-squares on F^2	Full-matrix least-squares on F^2
Data / restraints / parameters	694 / 65 / 82	796 / 65 / 91	1086 / 71 / 100	773 / 26 / 63
Goodness-of-fit	1.056	0.829	1.068	0.984
Final R indices [I > 2σ(I)]	R_{obs} = 0.0276, wR_{obs} = 0.0709	R_{obs} = 0.0290, wR_{obs} = 0.0641	R_{obs} = 0.0285, wR_{obs} = 0.0799	R_{obs} = 0.0637, wR_{obs} = 0.1496
R indices [all data]	R_{all} = 0.0348, wR_{all} = 0.0758	R_{all} = 0.0672, wR_{all} = 0.0684	R_{all} = 0.0434, wR_{all} = 0.0837	R_{all} = 0.1395, wR_{all} = 0.1964
Largest diff. peak and hole	1.587 and -1.861 e·$Å^{-3}$	0.903 and -1.627 e·$Å^{-3}$	1.238 and -1.954 e·$Å^{-3}$	6.944 and -2.056 e·$Å^{-3}$

Table S2 | Effective lattice parameter. a is the real lattice parameter whereas L correspond to the effective parameter , which is essentially the distance between two in-plane neighboring Pb atoms.

3D α-phase $FAPbI_3$, cubic Pm-3m	a=L
FA DJ n=2 to n=4, tetragonal, P4/mmm	a=L
DJ n=1, tetragonal, P4/mbm	$\frac{a}{\sqrt{2}} = L$
DJ n=1, monoclinic, $P2_1/c$	$\sqrt{ab}/2 = L$

Table S3 | Extracted PL linewidth and fitting parameters of FA DJ perovskites.
The extracted values for inhomogeneous exciton linewidth (Γ_0), strength of LO phonon coupling (Γ_{LO}), and LO phonon energy (E_{LO}) are listed for n = 2 and n = 3 perovskites, along with those reported for 3D $FAPbI_3$ films and nanocrystals.[5,16] The parameters are fitted using the formula of section 1.4.

Sample	**Γ_0 (meV)**	**Γ_{LO} (meV)**	**E_{LO} (meV)**
n=2	29.6 ± 0.5	20 ± 4	8.5 ± 1.2
n=3	24.5 ± 1.6	56 ± 22	18.2 ± 4.9
$FAPbI_3$	19 ± 1	40 ± 5	11.5 ± 1.2
$FAPbI_3$ (NC)	1.5	27	10.7

Table S4 | Optical dielectric constant (ε∞) and electronic band gaps (Eg). Optical dielectric constant (ε_∞) calculated within DFPT, and electronic band gaps (E_g) using the DSH hybrid functional, for the FA DJ series and for $FAPbI_3$, with (1.31) and without (1.07) the correction due to polymorphism.

	ε_∞ (PBE)	**E_g (DSH)**
n=1	5.18	1.93
n=2	5.76	1.69
n=3	6.04	1.50
n=4	6.20	1.42
FAPbI3	6.97	1.07
poly-FAPbI3	6.87	1.31

4. Methods

4.1 Crystal synthesis

Reagents: PbO (99.9%), hydroiodic acid (HI, 57 wt % in H2O, distilled, stabilized, 99.95%), hypophosphorous acid solution (H_3PO_2, 50 wt % in H2O) were purchased from Sigma-Aldrich. 3-(aminomethyl)piperidine (3AMP, 98%) was purchased from TCI, formamidinium chloride (FACl) was purchased from Great cell solar. All chemicals were used as received.

Synthesis of (3AMP)$(FA)_{n-1}Pb_nI_{3n+1}$, n=1 (Large batch powder crystal): For n=1, PbO powder (223.2 mg, 1mmol) was dissolved in a mixture of 57% w/w aqueous HI solution (5.0 mL, 39.2 mmol) at room temperature (25 °C) under constant magnetic stirring for 10 mins, which formed a bright yellow solution (PbI_2). In a separate beaker, 3AMP (101.6 μL, 0.85 mmol) was neutralized with H_3PO_2 50 wt % in aqueous (1.0 mL, 9.1 mmol) in an ice bath resulting in a clear colorless solution. Then the 3AMP solution was added into the PbI_2 solution under heating at 230 ℃ (hotplate temperature) with constant stirring. The addition initially produced red precipitates, which were slowly dissolved under heating. Then the solution was cooled down to room temperature and red needle-like crystals precipitated. The product n=1 sometime contains both monoclinic phase and tetragonal phase. If the crystal is heated up to 190 ℃, it will be locked at tetragonal phase even after being cooled down to room temperature (Fig. S1).

Synthesis of (3AMP)$(FA)_{n-1}Pb_nI_{3n+1}$, n=2-3 (Large batch powder crystal): Since the FACl is highly hygroscopic, it was stored and weighed in the glovebox under inert conditions.

For n=2, firstly, FACl (483mg, 6 mmol) was added in to a 50 ml glass conical flask sealed with a glass stopper prior to removal from the glovebox. The subsequent steps were conducted on a hot plate with vigorous stirring inside a fume hood. The glass stopper was removed and 57% wt % aqueous HI solution (20.0 mL, 152 mmol) and H_3PO_2 50 wt % aqueous (2.0 mL, 18.2 mmol) were quickly added to dissolve the FACl until a clear yellow solution was obtained. PbO powder (2678.4 mg, 12 mmol) was added into the FACl solution to form a yellow suspension at room temperature, then the hotplate was set to 230 ℃ (500 RPM stirring), until the color of suspension turned black. In a second beaker, 3AMP (427.4 μL, 3.6 mmol) was neutralized with 50 wt % aqueous H_3PO_2 (3.0 mL, 27.3 mmol) in an ice bath resulting in a clear colorless solution. Then the 3AMP/ H_3PO_2 solution was added into the black suspension in the first flask with vigorous stirring, within 1~2 minutes a clear yellow solution was obtained and it was further stirred for 5 mins. From this point, the temperature of hotplate was turned down to 120 ˚C (cooling rate of our ceramic hotplate is around 1 ˚C/4s). After the temperature reached 120 C, the solution was left at this temperature for 1 hour, and dark-red plate-like crystal slowly precipitated out. The crystal was then isolated rapidly without further cooling by suction filtration, followed by drying on the filtration funnel for a further 5 min. Finally, the crystal was put in a clean vial and dried in vacuum at 60 ℃ overnight.

For n=3, firstly, FACl (655mg, 8.1 mmol) was added in to a 50 ml glass conical flask sealed with a glass stopper prior to removal from the glovebox. The subsequent steps were conducted on a hot plate with vigorous stirring inside a fume hood. The glass stopper was removed, H_3PO_2 50

wt % aqueous (2.0 mL, 18.2 mmol) and 57% wt % aqueous HI solution (18.0 mL, 136.8 mmol) were quickly added to dissolve the FACl until a clear yellow solution was obtained. PbO powder (2566.8 mg, 11.5 mmol) was added into the FACl solution to form a yellow suspension at room temperature, then the hotplate was set to 230 °C (500 RPM stirring), until the color of suspension turned black. In a second beaker, 3AMP (150 μL, 1.3 mmol) was neutralized with 50 wt % aqueous H_3PO_2 (4.0 mL, 36.4 mmol) in an ice bath resulting in a clear colorless solution. Then the 3AMP/ H_3PO_2 solution was added into the black suspension in the first flask with vigorous stirring, within 1~2 minutes a clear yellow solution was obtained and it was further stirred for 5 mins. From this point, the temperature of hotplate was turned down to 120 ˚C (cooling rate of our ceramic hotplate is around 1 ˚C/4s). After the temperature reaches 120 ˚C, the solution is left at this temperature for 1 hour, and black plate-like crystal slowly precipitated out. The crystal was then isolated rapidly without further cooling by suction filtration, followed by drying on the filtration funnel for a further 5 min. Finally, the crystal was put in a clean vial and dried in vacuum at 60 °C overnight.

To avoid the corrosion of the vacuum oven (mostly made of steel), crystal can be washed using heptane to get rid of the residue HI before drying in the oven. (Certainly, this washing is optional.)

Synthesis of n=1, n=2 and n=3 powders are highly reproducible and scalable. For powder synthesis of n=4, we found it is hard to obtain pure product as the yellow, δ-phase $FAPbI_3$ always form together as the impurity. We were only able to synthesize pure n=4 using a previously reported KCSC method, which is introduced below. However, it is small single crystal (up to mm size or smaller) and not scalable. More discussion on the synthesis can be found in SI section 1.3.

Synthesis of $(3AMP)(FA)_{n-1}Pb_nI_{3n+1}$, n=4 (thin large crystal): The n=4 large thin crystal was synthesized using our previous reported kinetically controlled space confinement (KCSC) method.[4] First, solution of n=3 was prepared using the stoichiometry introduced above. After the addition of 3AMP/ H_3PO_2 solution was added into the black suspension in the first flask, yellow solution was obtained. From this point, instead of cooling it down, 1ml of boiling yellow solution is taken out and added in to 500 μL HI solution (57% wt % aqueous) in a separate vial.

Glass was used as the substrate for the 2D perovskite growth. Glass substrates were cut into 1-inch* 1-inch squares, cleaned in soap water, acetone, isopropanol by ultrasonication for 20 min each; then dried by argon. The substrates were transferred into a UV-Ozone cleaner and cleaned for 10 mins. The substrates were put on a hot plate, 12.5 μL of the parent solution was dropped onto the glass surface, another glass slide was put on top to fully cover the bottom glass and annealed at 80 °C for 7 hours. Then the top glass is removed, the crystal with the bottom glass is placed on spin coater, heptane as the washing solvent was dropped (80 μl) instantly on the crystal while spin coated at 3000 r.p.m for 30 seconds to remove all the residue parent acid solution.

The synthesis n=4 is not as reproducible as the lower n, sometimes multiple attempts are necessary. Yellow needle-like crystal, which is $NH_4PbI_3{\cdot}2H_2O$, could be observed[17] occasionally

as impurity if the reaction period is too long, as the partial decomposition of formamidine to ammonia in acidic media.[18–20]

This method for synthesis of large thin crystal is applicable to n=1 to n=3. Each of them uses the solution with corresponding stoichiometry. Specifically, for n=1 large thin crystal, solution of n=1 was prepared using the stoichiometry introduced above, and then annealed at 70 °C for 5 hours; For n=2 crystal, solution of n=2 was prepared using the stoichiometry introduced above, and then annealed at 70 °C for 4 hours; For n=3 crystal, solution of n=3 was prepared using the stoichiometry introduced above, and then annealed at 70 °C for 4 hours.

4.2 Construction of a Schematic Phase Diagram

The schematic phase diagram shown in Fig. 1d was created from a simple model of the Gibbs free energy of the various phases present in the perovskite solution (DJ n=1-4, δ-$FAPbI_3$, α-$FAPbI_3$, and a solvated phase). Free energies were plotted together on a HI-DJ n1-$FAPbI_3$ ternary plot, and the corresponding ternary phase diagram was obtained from the convex hull of this free energy landscape. Crystalline phases were given Kronecker delta – like free energy functions positioned at their crystal stoichiometry, with the height of the delta tuned to reproduce the observed order of crystal growth from solution (|G(DJ n2)| > |G(n3)| > |G(n4)| > |G(n1)| > |G(α-$FAPbI_3$)|). The free energy of these phases was taken to be temperature-invariant, while |G(δ -$FAPbI_3$)| was made to decrease from |G(DJ n2)| to 0 with temperature. The free energy of the solution phase was taken to be a convex function with a maximum near the center of the ternary plot and zeros at the corners and along the DJ – $FAPbI_3$ edge. The magnitude of the solution-phase free energy was increased with temperature.

The ternary phase diagram constructed from the free energy of these phases was made to evolve with temperature. A horizontal line (a line of constant [HI]) across the ternary phase diagram was chosen to represent the solution concentration, and the intersection of each region of the phase diagram with this line was tracked as temperature was increased. In this way the binary phase diagram representing FA DJ at a specific concentration in HI solution was constructed. The process of creating the binary phase diagram from ternary phase diagrams is shown in Fig. S4.

4.3 1D X-ray diffraction measurements

The measurements were conducted using a Rigaku Smartlab II X-Ray diffractometer with Cu(Kα) radiation (λ = 1.5406 Å), running at 40 kV and 44 mA.

4.4 Single crystal structure measurements

Intensity data of a black plate single crystal of thick-layered perovskite containing 3AMP were collected at 293 K. A suitable single crystal with dimensions of ~0.1×0.1×0.02 mm3 was mounted on a MiTeGen loop with Paratone oil on a STOE StadiVari diffractometer equipped with an AXO Ag Kα micro-focus sealed Xray A-MiXS source (λ = 0.560834 Å), running at 65 kV and 0.68 mA, and a Dectris Pilatus3 R CdTe 300K Hybrid Photon Counting detector. Data reduction was performed with the CrysAlisPro software using a spherical absorption correction. The structure was solved with the ShelXT structure solution program using the Intrinsic Phasing

solution method and by using Olex2 as the graphical interface. The model was refined with ShelXL using least squares minimization.

4.5 Absorbance measurements

The optical absorbance measurements were conducted using a broad-band light source (Thorlabs Solis-3C) focused onto the sample with a 50 μm beam size. The transmitted spectrum was collected by optical fiber and then sent to the spectrometer (Andor Kymera 328i) and CCD (Andor iDus 416). The measurement was conducted on thin KCSC crystals.

4.6 PL measurements

The photoluminescence (PL) spectroscopy of FA DJ 2D perovskites was measured based on a lab-built confocal microscopy system. The sample was photo-excited at 480nm using a supercontinuum pulsed laser (repetition rate 78MHz, temporal width ~50ps, NKT Photonics) spectral selected at 480nm. The laser was focused onto the sample through a 50x objective (0.42 NA) with ~ 1um beam size, yielding an excitation intensity of 3.6×10^4 mW/cm^2. The PL data was collected from 500 to 950 nm (1.3-2.4eV) by a spectrometer (Andor Kymera 328i) and a CCD camera (Andor iDus 416). For room temperature PL measurements, the sample was kept and measured at ambient condition. For temperature-dependent PL spectroscopy, the sample was kept under vacuum (10^{-4} to 10^{-5} torr) in a closed-cycle cryostat (Advanced Research Systems) with sample temperature range from 6.5K to 300K using a temperature controller (Lakeshore). The excitation intensity was kept the same for all temperature ranges.

The temperature-dependent reflectance measurements were carried out in the same microscopy system, with the broad-band white light source (Thorlabs Solis-3C) focused on the sample guided by a beam splitter. The reflected spectra were normalized by reflectance of silver mirror on the sample plane.

4.7 1D and 2D NMR

The 3D a-$FAPBI_3$ and 2D RP and DJ materials were separately packed into 1.3 mm (outer diameter) zirconia rotors fitted with VESPEL caps without any further sample pretreatment. Solid-state MAS NMR experiments were conducted on a 21.1 T (Larmor frequencies of ^{1}H and ^{207}Pb were 900.2 MHz and 188.6 MHz, respectively) Bruker AVANCE-NEO spectrometer using a double resonance 1.3 mm H-X probehead. Unless specified, the MAS frequency was 50 kHz in all ssNMR experiments. The 1D ^{1}H MAS NMR spectra were acquired by co-addition of 16 transients, where the relaxation delays were optimized to ensure the quantitate analysis of peak integrals. The spin-lattice relaxation time (T_1) values are determined from saturation recovery measurements and analyses. Echo-detected 1D ^{207}Pb MAS NMR experiments were carried out with 40960 co-added transients, using 1 rotor-period echo delay (20 microseconds) with a repletion delay of 1.2 s, leading to an experimental time of 14 h each. All 2D ^{1}H-^{1}H spin diffusion NMR experiments were acquired using three-pulse noesy-like sequence under fast MAS with 50 ms and 500 ms of mixing times. A rotor-synchronized increment of 20 microseconds was applied to detect 400 t_1 increments. The ^{1}H experimental shift was calibrated

with respect to neat TMS using adamantane as an external reference (^{1}H resonance, 1.82 ppm). All spectra were processed using Bruker Topspin 4.1 inbuilt package.

4.8 Low-frequency Raman measurement

Raman spectroscopy measurements were carried out using a diode laser module stabilized by volume holographic grating (VHG) filter, operating at 830nm (Coherent Ondax THz-Raman). The excitation laser was introduced into a home-built microscope and focused onto the sample using a microscope objective (Nikon ELWD 20x, NA 0.45). Typical laser power on sample surface was 2.4 mW. The light retro-reflected from the sample was routed back into the laser module which integrates a set of VHG notch filters. The Rayleigh scattered light was attenuated by the VHG filter set. The remaining Raman scattered light was subsequently fiber coupled into a spectrometer (Princeton Instruments Iso-Plane 320), dispersed by a 1200 grooves/mm grating, and captured by a thermoelectrically cooled CCD camera (PIXIS-BRX400). Typical integration time was 100s.

4.9 Computational methods

DFT calculations for obtaining the PDF, phonon spectral functions, and DOS were performed using the Quantum Espresso (QE) software[21,22]. A kinetic energy cutoff of 120 Ry, the PBEsol approximation[23], and optimized norm-conserving Vanderbilt pseudopotentials[24] were used. To obtain the polymorphous structures[10] we follow the method described in Ref. [25]. We employ 2x2x2 and 2x2x1 supercells of the primitive cells of cubic $FAPbI_3$ and (3AMP)$FAPb_2I_7$ containing 96 and 164 atoms, respectively. Geometry optimizations in supercells were performed by allowing the nuclear coordinates to relax and keeping the lattice constants fixed to their experimental values. We employed 3x3x3 and 3x3x2 uniform k-grids to sample the Brillouin Zone of polymorphous cubic $FAPbI_3$ and (3AMP)$FAPb_2I_7$. Geometry optimizations and phonon calculations (see below) were performed using scalar relativistic pseudopotentials, neglecting the effect of spin-orbit coupling.

Doubly Screened Hybrid: We perform density functional based calculation with the projector augmented wave potentials[26] as implemented in the VASP code[27]. The energy cut-off for the expansion of the wave-functions is set at 450 eV, and spin-orbit coupling interactions were taken into account for all calculations. To maintain the symmetry of the structures, we proceed to replace the organic moieties with Cs atoms that were placed at the position of the N-atoms. We checked that this replacement is not affecting the electronic structure by comparing the band structures, and that no symmetry is broken (i.e., the space group remains the same as the experimentally observed). Furthermore, to include the effect of polymorphism is the structures, we also performed a calculation of a 2x2x2 super-cell of $FAPbI_3$ (poly-$FAPbI_3$) which include the FA molecules. To overcome the well-known band-gap underestimation of DFT, we employ the doubly screened hybrid exchange-correlation functional.[28–30] We calculate from first-principles the ε_∞ (details below) for all compounds and use ε^{-1}_∞ as the mixing parameter for the long range, while the exact exchange is used for the short range. For the employed model dielectric function, we used a screening length parameter μ value of 1.05, which was taken from GW_o calculations of Bokdam et al. on $FAPbI_3$.[31] For the calculations of the exact exchange we employed uniform Γ-centered k-point grids of 4x4x2 for the layered materials, and 6x6x6 (2x2x2) for the mono-$FAPbI_3$ and poly-$FAPbI_3$, respectively.

***Calculation of ε_∞*:** We used the density functional perturbation theory (DFPT) to calculate the dielectric constant of the n=1,2,3,4, mono-$FAPbI_3$ and poly- $FAPbI_3$ compounds. We employed Γ-centered k-point grids of 12x12x4, 12x12x4, 10x10x4,10x10x4, 20x20x20 and 6x6x6, respectively. Local field effects were included at the DFT level. For the layered materials we replaced the organic spacers with N atoms,

thus to avoid artifacts due to the different dielectric screening, we used a capacitor stack model to extract the ε_∞ of the inorganic slab layer from the DFPT calculation.[28,32] The final ε_∞ for the materials are given in Table S4.

4.10 Phonons and PDF

The phonons of the polymorphous structures were calculated by means of finite differences using the zeroth order iteration of the anharmonic special displacement method (A-SDM)[33]. PDFs of the polymorphous structures were evaluated as

$$G(\tau) = \frac{1}{\tau}\sum\sum\delta\left(\tau - \tau_{\kappa\kappa\prime}\right)$$

by replacing the delta function with a Gaussian of width 0.035 Angstroms. Here, κ is the atom index and $\tau_{\kappa\kappa'}$ defines the distance between atom κ and κ'. To include the effect of thermal vibrations in the PDFs we employed thermally displaced configurations in 10x10x10 and 20x20x1 supercells. The configurations were generated using the A-SDM at essentially no cost, as it takes advantage of Fourier interpolation of the phonons in the reciprocal space.[34]

4.11 Phonon spectral functions

Phonon spectral functions were calculated using the phonon unfolding technique[25] as implemented in the ZG package of EPW.[35] We employed 663 and 787 equally-spaced **q**-points for (3AMP)$FAPb_2I_7$ and $FAPbI_3$, respectively, and 12 × 12 × 12 **g**-grid of reciprocal lattice vectors to ensure convergence of the spectral weights.

4.12 DOS at finite temperatures

Electronic structure calculations for the DOS were performed using fully relativistic pseudopotentials, including the effect of spin-orbit coupling. To calculate the DOS at the VBM and CBM for 300 K, we employed the A-SDM. In the A-SDM, anharmonic phonons computed for the polymorphous structures are used to generate thermally displaced configurations, which capture the effect of electron-phonon coupling on the electronic structure when combined with DFT calculations.[25] To obtain the DOS of polymorphous $FAPbI_3$ and (3AMP)$FAPb_2I_7$ at 300 K we used 10 configurations of supercell size 4x4x4 (768 atoms) and 4x4x1 (656 atoms), respectively. We used 1x1x1 and 1x1x2 grids to sample the Brillouin zone of these supercells. The phonon-induced band gap renormalization, $\Delta\varepsilon_g$, with respect to the band gap of the polymorphous structure at static-equilibrium was determined by taking the average renormalization over the 10 configurations.

4.13 PL diffusion measurements

Montana Instruments Cryostation, with attached turbo pump, was employed to maintain a high vacuum environment (10^{-4} to 10^{-5} Torr) during room temperature (295 K) measurements. An objective with 100× magnification and 0.9 NA focused a 532 nm continuous-wave laser onto the samples with a resulting beam diameter (D4σ) of ~ 0.6 μm. A neutral density filter was placed in the beam path, before the objective, to modulate the laser power for the power-dependent measurements. Laser contributions from the reflected PL were blocked with a 550 nm long-pass filter, installed before the detector. Additionally, free carrier diffusion contributions were removed with a 700 nm short-pass filter for both n=2 and n=3 FA DJ perovskites. Subsequent real-space emission images of the sample surface were acquired using an

EMCCD camera in low electron multiplication mode[36]. An n-type GaAs wafer was used for calibration of measurements and to confirm reliability of analysis.

4.14 Time-resolved Photoluminescence

The TRPL spectrum of DJ n=3 sample was acquired with a lab-built confocal microscopy system. The sample was photo-excited using a 50-ps-pulsed super-continuum laser (NKT Photonics, repetition rate tuned at 39MHz) spectral selected at 480 nm. The excitation laser was focused onto the sample with ~ 1um beam size and average excitation intensity of 1.8×10^4 mW/cm^2. The emission was collected using PicoQuant HydraHarp 400 time-correlated single photon counting system combined with an Avalanche Photo-Diode (MPD-SPAD). The emission was spectrally filtered through a spectrograph (Andor Kymera 328i) to remove laser excitation. During TRPL measurement, the sample was kept under vacuum (10^{-4} to 10^{-5} torr) in a closed-cycle cryostat and maintained at cryogenic temperature (T = 6.5K).

Reference:

(1) Roy, C. R.; Zhou, Y.; Kohler, D. D.; Zhu, Z.; Wright, J. C.; Jin, S. Intrinsic Halide Immiscibility in 2D Mixed-Halide Ruddlesden–Popper Perovskites. *ACS Energy Lett.* **2022**, *7* (10), 3423–3431. https://doi.org/10.1021/acsenergylett.2c01631.

(2) Li, X.; Hoffman, J. M.; Kanatzidis, M. G. The 2D Halide Perovskite Rulebook: How the Spacer Influences Everything from the Structure to Optoelectronic Device Efficiency. *Chem. Rev.* **2021**, *121* (4), 2230–2291. https://doi.org/10.1021/acs.chemrev.0c01006.

(3) Vasileiadou, E. S.; Wang, B.; Spanopoulos, I.; Hadar, I.; Navrotsky, A.; Kanatzidis, M. G. Insight on the Stability of Thick Layers in 2D Ruddlesden–Popper and Dion–Jacobson Lead Iodide Perovskites. *Journal of the American Chemical Society* **2021**, *143* (6), 2523–2536.

(4) Hou, J.; Li, W.; Zhang, H.; Sidhik, S.; Fletcher, J.; Metcalf, I.; Anantharaman, S. B.; Shuai, X.; Mishra, A.; Blancon, J.-C.; Katan, C.; Jariwala, D.; Even, J.; Kanatzidis, M. G.; Mohite, A. D. Synthesis of 2D Perovskite Crystals via Progressive Transformation of Quantum Well Thickness. *Nat. Synth* **2024**, *3* (2), 265–275. https://doi.org/10.1038/s44160-023-00422-3.

(5) Wright, A. D.; Verdi, C.; Milot, R. L.; Eperon, G. E.; Pérez-Osorio, M. A.; Snaith, H. J.; Giustino, F.; Johnston, M. B.; Herz, L. M. Electron–Phonon Coupling in Hybrid Lead Halide Perovskites. *Nat Commun* **2016**, *7* (1), 11755. https://doi.org/10.1038/ncomms11755.

(6) Fu, P.; Quintero, M. A.; Welton, C.; Li, X.; Cucco, B.; De Siena, M. C.; Even, J.; Volonakis, G.; Kepenekian, M.; Liu, R.; Laing, C. C.; Klepov, V.; Liu, Y.; Dravid, V. P.; Manjunatha Reddy, G. N.; Li, C.; Kanatzidis, M. G. Short Aromatic Diammonium Ions Modulate Distortions in 2D Lead Bromide Perovskites for Tunable White-Light Emission. *Chem. Mater.* **2022**, *34* (21), 9685–9698. https://doi.org/10.1021/acs.chemmater.2c02471.

(7) Fu, P.; Quintero, M. A.; Vasileiadou, E. S.; Raval, P.; Welton, C.; Kepenekian, M.; Volonakis, G.; Even, J.; Liu, Y.; Malliakas, C.; Yang, Y.; Laing, C.; Dravid, V. P.; Reddy, G. N. M.; Li, C.; Sargent, E. H.; Kanatzidis, M. G. Chemical Behavior and Local Structure of the Ruddlesden–Popper and Dion–Jacobson Alloyed Pb/Sn Bromide 2D Perovskites. *J. Am. Chem. Soc.* **2023**, *145* (29), 15997–16014. https://doi.org/10.1021/jacs.3c03997.

(8) Dahlman, C. J.; Kubicki, D. J.; Reddy, G. M. Interfaces in Metal Halide Perovskites Probed by Solid-State NMR Spectroscopy. *Journal of Materials Chemistry A* **2021**, *9* (35), 19206–19244.

(9) Lee, J.; Lee, W.; Kang, K.; Lee, T.; Lee, S. K. Layer-by-Layer Structural Identification of 2D Ruddlesden–Popper Hybrid Lead Iodide Perovskites by Solid-State NMR Spectroscopy. *Chem. Mater.* **2021**, *33* (1), 370–377. https://doi.org/10.1021/acs.chemmater.0c04078.

(10) Zhao, X.-G.; Dalpian, G. M.; Wang, Z.; Zunger, A. Polymorphous Nature of Cubic Halide Perovskites. *Physical Review B* **2020**, *101* (15), 155137.

(11) Laurita, G.; Fabini, D. H.; Stoumpos, C. C.; Kanatzidis, M. G.; Seshadri, R. Chemical Tuning of Dynamic Cation Off-Centering in the Cubic Phases of Hybrid Tin and Lead Halide Perovskites. *Chemical Science* **2017**, *8* (8), 5628–5635.
(12) Cadiz, F.; Robert, C.; Courtade, E.; Manca, M.; Martinelli, L.; Taniguchi, T.; Watanabe, K.; Amand, T.; Rowe, A. C. H.; Paget, D.; Urbaszek, B.; Marie, X. Exciton Diffusion in WSe2 Monolayers Embedded in a van Der Waals Heterostructure. *Applied Physics Letters* **2018**, *112* (15), 152106. https://doi.org/10.1063/1.5026478.
(13) Xiao, X.; Wu, M.; Ni, Z.; Xu, S.; Chen, S.; Hu, J.; Rudd, P. N.; You, W.; Huang, J. Ultrafast Exciton Transport with a Long Diffusion Length in Layered Perovskites with Organic Cation Functionalization. *Advanced Materials* **2020**, *32* (46), 2004080. https://doi.org/10.1002/adma.202004080.
(14) Quarti, C.; Katan, C.; Even, J. Physical Properties of Bulk, Defective, 2D and 0D Metal Halide Perovskite Semiconductors from a Symmetry Perspective. *Journal of Physics: Materials* **2020**, *3* (4), 042001.
(15) Li, J.; Yu, Q.; He, Y.; Stoumpos, C. C.; Niu, G.; Trimarchi, G. G.; Guo, H.; Dong, G.; Wang, D.; Wang, L.; Kanatzidis, M. G. Cs2PbI2Cl2, All-Inorganic Two-Dimensional Ruddlesden–Popper Mixed Halide Perovskite with Optoelectronic Response. *J. Am. Chem. Soc.* **2018**, *140* (35), 11085–11090. https://doi.org/10.1021/jacs.8b06046.
(16) Fu, M.; Tamarat, P.; Trebbia, J.-B.; Bodnarchuk, M. I.; Kovalenko, M. V.; Even, J.; Lounis, B. Unraveling Exciton–Phonon Coupling in Individual FAPbI3 Nanocrystals Emitting near-Infrared Single Photons. *Nat Commun* **2018**, *9* (1), 3318. https://doi.org/10.1038/s41467-018-05876-0.
(17) Bedlivy, D.; Mereiter, K. The Structures of Potassium Lead Triiodide Dihydrate and Ammonium Lead Triiodide Dihydrate. *Acta Crystallographica Section B* **1980**, *36* (4), 782–785. https://doi.org/10.1107/S0567740880004529.
(18) Stoumpos, C. C.; Malliakas, C. D.; Kanatzidis, M. G. Semiconducting Tin and Lead Iodide Perovskites with Organic Cations: Phase Transitions, High Mobilities, and Near-Infrared Photoluminescent Properties. *Inorg. Chem.* **2013**, *52* (15), 9019–9038. https://doi.org/10.1021/ic401215x.
(19) Schaefer, F. C.; Hechenbleikner, I.; Peters, G. A.; Wystrach, V. P. Synthesis of the Sym-Triazine System. I. Trimerization and Cotrimerization of Amidines. *J. Am. Chem. Soc.* **1959**, *81* (6), 1466–1470. https://doi.org/10.1021/ja01515a046.
(20) Hinkel, L. E.; Dunn, R. T. CCXXXVII.—Studies on Hydrogen Cyanide. Part II. The Compounds Formed by the Action of the Hydrogen Halides on Hydrogen Cyanide. *J. Chem. Soc.* **1930**, No. 0, 1834–1839. https://doi.org/10.1039/JR9300001834.
(21) Giannozzi, P.; Andreussi, O.; Brumme, T.; Bunau, O.; Nardelli, M. B.; Calandra, M.; Car, R.; Cavazzoni, C.; Ceresoli, D.; Cococcioni, M. Advanced Capabilities for Materials Modelling with Quantum ESPRESSO. *Journal of physics: Condensed matter* **2017**, *29* (46), 465901.
(22) Giannozzi, P.; Baroni, S.; Bonini, N.; Calandra, M.; Car, R.; Cavazzoni, C.; Ceresoli, D.; Chiarotti, G. L.; Cococcioni, M.; Dabo, I. QUANTUM ESPRESSO: A Modular and Open-Source Software Project for Quantum Simulations of Materials. *Journal of physics: Condensed matter* **2009**, *21* (39), 395502.
(23) Perdew, J. P.; Ruzsinszky, A.; Csonka, G. I.; Vydrov, O. A.; Scuseria, G. E.; Constantin, L. A.; Zhou, X.; Burke, K. Generalized Gradient Approximation for Solids and Their Surfaces. *arXiv preprint arXiv:0707.2088* **2007**.
(24) Hamann, D. R. Optimized Norm-Conserving Vanderbilt Pseudopotentials. *Physical Review B* **2013**, *88* (8), 085117.
(25) Zacharias, M.; Volonakis, G.; Giustino, F.; Even, J. Anharmonic Electron-Phonon Coupling in Ultrasoft and Locally Disordered Perovskites. *npj Computational Materials* **2023**, *9* (1), 153.
(26) Blöchl, P. E. Projector Augmented-Wave Method. *Phys. Rev. B* **1994**, *50* (24), 17953–17979. https://doi.org/10.1103/PhysRevB.50.17953.

(27) Kresse, G.; Joubert, D. From Ultrasoft Pseudopotentials to the Projector Augmented-Wave Method. *Phys. Rev. B* **1999**, *59* (3), 1758–1775. https://doi.org/10.1103/PhysRevB.59.1758.
(28) Garba, I. B.; Trombini, L.; Katan, C.; Even, J.; Zacharias, M.; Kepenekian, M.; Volonakis, G. Three-Dimensional to Layered Halide Perovskites: A Parameter-Free Hybrid Functional Method for Predicting Electronic Band Gaps. arXiv January 23, 2025. https://doi.org/10.48550/arXiv.2501.13852.
(29) Chen, W.; Miceli, G.; Rignanese, G.-M.; Pasquarello, A. Nonempirical Dielectric-Dependent Hybrid Functional with Range Separation for Semiconductors and Insulators. *Phys. Rev. Mater.* **2018**, *2* (7), 073803. https://doi.org/10.1103/PhysRevMaterials.2.073803.
(30) Cui, Z.-H.; Wang, Y.-C.; Zhang, M.-Y.; Xu, X.; Jiang, H. Doubly Screened Hybrid Functional: An Accurate First-Principles Approach for Both Narrow- and Wide-Gap Semiconductors. *J. Phys. Chem. Lett.* **2018**, *9* (9), 2338–2345. https://doi.org/10.1021/acs.jpclett.8b00919.
(31) Bokdam, M.; Sander, T.; Stroppa, A.; Picozzi, S.; Sarma, D. D.; Franchini, C.; Kresse, G. Role of Polar Phonons in the Photo Excited State of Metal Halide Perovskites. *Sci Rep* **2016**, *6* (1), 28618. https://doi.org/10.1038/srep28618.
(32) Sio, W. H.; Giustino, F. Unified Ab Initio Description of Fr\"ohlich Electron-Phonon Interactions in Two-Dimensional and Three-Dimensional Materials. *Phys. Rev. B* **2022**, *105* (11), 115414. https://doi.org/10.1103/PhysRevB.105.115414.
(33) Zacharias, M.; Volonakis, G.; Giustino, F.; Even, J. Anharmonic Lattice Dynamics via the Special Displacement Method. *Phys. Rev. B* **2023**, *108* (3), 035155. https://doi.org/10.1103/PhysRevB.108.035155.
(34) Zacharias, M.; Giustino, F. Theory of the Special Displacement Method for Electronic Structure Calculations at Finite Temperature. *Physical Review Research* **2020**, *2* (1), 013357.
(35) Lee, H.; Poncé, S.; Bushick, K.; Hajinazar, S.; Lafuente-Bartolome, J.; Leveillee, J.; Lian, C.; Lihm, J.-M.; Macheda, F.; Mori, H. Electron–Phonon Physics from First Principles Using the EPW Code. *npj Computational Materials* **2023**, *9* (1), 156.
(36) Chand, S. B.; Woods, J. M.; Quan, J.; Mejia, E.; Taniguchi, T.; Watanabe, K.; Alù, A.; Grosso, G. Interaction-Driven Transport of Dark Excitons in 2D Semiconductors with Phonon-Mediated Optical Readout. *Nat Commun* **2023**, *14* (1), 3712. https://doi.org/10.1038/s41467-023-39339-y.